Eliminating error in the chemical abundance scale for extragalactic H II regions

Á. R. López-Sánchez,[1,2]* M. A. Dopita,[3,4,5] L. J. Kewley,[5] H. J. Zahid,[5] D. C. Nicholls[3] and J. Scharwächter[3]

[1]*Australian Astronomical Observatory, PO Box 296, Epping, NSW 1710, Australia*
[2]*Department of Physics and Astronomy, Macquarie University, NSW 2109, Australia*
[3]*Research School of Astronomy and Astrophysics, Australian National University, Cotter Road, Weston, ACT 2611, Australia*
[4]*Astronomy Department, Faculty of Science, King Abdulaziz University, PO Box 80203, Jeddah 21589, Saudi Arabia*
[5]*Institute for Astronomy, University of Hawaii, 2680 Woodlawn Drive, Honolulu, HI 96822, USA*

ABSTRACT

In an attempt to remove the systematic errors which have plagued the calibration of the H II region abundance sequence, we have theoretically modelled the extragalactic H II region sequence. We then used the theoretical spectra so generated in a double-blind experiment to recover the chemical abundances using both the classical electron temperature + ionization correction factor technique and the technique which depends on the use of strong emission lines (SELs) in the nebular spectrum to estimate the abundance of oxygen. We find a number of systematic trends, and we provide correction formulae which should remove systematic errors in the electron temperature + ionization correction factor technique. We also provide a critical evaluation of the various semi-empirical SEL techniques. Finally, we offer a scheme which should help to eliminate systematic errors in the SEL-derived chemical abundance scale for extragalactic H II regions.

Key words: methods: data analysis – techniques: spectroscopic – ISM: abundances – H II regions – galaxies: abundances.

1 INTRODUCTION

To understand how galaxies in the early Universe evolved into those that we see locally requires an understanding of both the chemical and star formation history of galaxies over cosmic time. Indeed, observational data compiling hundreds of thousands of galaxies at different redshifts are suggesting that there actually is a deep physical connection between metallicities, masses and star formation rate (e.g. Brinchmann et al. 2004; Tremonti et al. 2004; Kewley & Ellison 2008; Lara-López et al. 2010a,b), although these results are mainly based on trends of the chemical abundances and not on their absolute metallicities.

Theoretical simulations can now predict the evolution of chemical abundances in galaxies (e.g. Mollá & Díaz 2005; Davé & Oppenheimer 2007). However, it is difficult to put these predictions to the test because the absolute calibration of the chemical abundance scale from H II regions is currently discrepant by more than a factor of 2. See, for example, the work of Kewley & Ellison

(2008) where abundances were calculated for 45 000 galaxies from the Sloan Digital Sky Survey (SDSS) (York et al. 2000; Abazajian et al. 2003) using 10 different calibrations given in the literature. Although all methods show some correlation with abundance, there is typically a scatter ranging over a factor of 2–3 in the absolute oxygen abundance derived from the various techniques. The same result was found by López-Sánchez & Esteban (2010), who also considered in their analysis the metallicities derived using a direct determination of the electron temperature of the ionized gas. Without a proper estimation of the absolute chemical abundances in galaxies, the comparison between observational data and theoretical models is not entirely satisfactory.

Thanks to its strong emission lines (SELs), the easiest element to measure in H II region emission spectra is oxygen. This is fortunate, since O is an α-process element made directly in short-lived massive stars. It comprises about 50 per cent of all the heavy elements by mass throughout the Universe, and is therefore representative of all the heavy elements. By contrast, Fe is made in lower mass stars, and is not released promptly into the interstellar medium of galaxies. The O/H abundance in H II regions is typically expressed in terms of 12+log(O/H), where O/H is the ratio of the number of oxygen to

*E-mail: alopez@aao.gov.au

hydrogen atomic density. This has been determined in three semi-empirical ways, as well as through direct theoretical photoionization modelling.

(1) By direct measurement of the electron temperature, from line ratios such as [O III] $\lambda 4363/\lambda 5007$ (see Osterbrook & Ferland 2006), followed by an analysis of the various ionization fractions in the zones of the H II region which produce optical emission lines. We dub this the T_e method. This has been very extensively applied by observers over the past 30 years (e.g. Peimbert & Costero 1969; Stasińska 1978; Aller 1984; Díaz et al. 1987; Izotov, Thuan & Lipovetski 1994; Esteban & Peimbert 1995; Vílchez & Esteban 1996; Esteban et al. 2004; Bresolin et al. 2005; Stasińska 2005; Izotov et al. 2006; López-Sánchez & Esteban 2009).

(2) By direct measurement of recombination lines (RLs) of ions of heavy elements such as O II and, in some cases, O I and comparing these with the RLs of hydrogen (e.g. Esteban et al. 1998, 2004, 2009; García-Rojas et al. 2004; García-Rojas & Esteban 2007; López-Sánchez et al. 2007; Peimbert et al. 2007). We refer to this technique as the RL method, although it is generally not useful in the determination of the cosmic abundance scale, since the RLs of heavy elements are generally too weak ($\sim 10^4$–10^6 times fainter than Hβ) to measure.

(3) By measurement of the SELs in the H II region spectrum calibrated using

(a) photoionization modelling (e.g. Pagel et al. 1979; McGaugh 1991; Kewley & Dopita 2002; Kobulnicky & Kewley 2004; Dopita et al. 2006a; Dors & Copetti 2006) or

(b) H II regions for which the oxygen abundance is known from the T_e method (e.g. Pilyugin 2001a,b; Denicoló, Terlevich & Terlevich 2002; Pettini & Pagel 2004; Pérez-Montero & Díaz 2005; Pilyugin & Thuan 2005; Pilyugin, Vílchez & Thuan 2010; Pilyugin & Mattsson 2011).

We will call this the SEL method, and it is nowadays extensively used to determine metallicities in large galaxy surveys.

Each of these methods has its particular problems and range of applications. More importantly, where all methods can be used, the derived O/H abundances often show systematic disagreements between the various methods. These may amount to factors of 2 or more. In this paper, we seek to resolve some of the causes of these discrepancies by rederiving the chemical abundances of model H II regions using the T_e method and the standard SEL techniques. We use a double-blind approach, so that the analysis of the photoionization models was conducted without any a priori knowledge of the chemical abundances and physical parameters used in the photoionization models.

We will now briefly indicate how these alarming abundance discrepancies between the various methods may arise.

1.1 The T_e and RL methods

At normal nebular temperatures ($T_e \sim 10^4$ K), the auroral [O III] $\lambda 4363$ line is only a few per cent as strong as the nebular $\lambda 5007$ line, so that high-quality spectra are required to give an adequate signal-to-noise ratio (S/N) to measure the fainter line. When the S/N is inadequate, the strength of the fainter line tends to be overestimated, leading to an underestimate in the derived abundance. This is also true for other commonly used temperature-sensitive line ratios.

A more insidious problem was first pointed out by Peimbert & Costero (1969). This still has not been resolved to everyone's satisfaction. Normal H II regions are not homogeneous but contain

temperature gradients, dense inclusions in which collisional de-excitation of cooling lines leads to higher temperatures, as well as colliding supersonic flows in which both density and electron temperatures may be raised as a result of shocks. In all such regions of enhanced temperature, the [O III] $\lambda 4363/\lambda 5007$ emission-line flux ratio is raised by a factor which depends only on the temperature. This would not be a problem except for the fact that the line emissivity is also raised in such regions by a factor proportional to the square of the electron density, n_e^2. Thus, the temperature estimate provided by the forbidden line ratio is dominated by the line ratio characterizing these overdense inclusions, rather than providing a measure of the electron temperature of the nebula as a whole. The electron temperature is therefore systematically overestimated. Hence, the presence of temperature gradients or fluctuations in the ionized gas leads to the abundances based on the T_e method being systematically underestimated (Peimbert 1967; Stasińska 2002, 2005; Peimbert et al. 2007).

Indeed, detailed studies that compared heavy element abundances derived using both the T_e method and the RL method in Galactic (Esteban et al. 2004; García-Rojas et al. 2005, 2006; García-Rojas & Esteban 2007; Mesa-Delgado et al. 2009b, 2011; Mesa-Delgado & Esteban 2010) and extragalactic (Peimbert 2003; Tsamis et al. 2003; López-Sánchez et al. 2007; Esteban et al. 2009) H II regions find a very good agreement between both results when temperature fluctuations are considered. However, their origin and existence are still controversial because they are not well reproduced by standard photoionization models (Kingdon & Ferland 1995; Rodríguez & García-Rojas 2010), and hence additional mechanisms are proposed to explain the presence of temperature fluctuations in the ionized gas (see reviews by Esteban 2002; Peimbert & Peimbert 2006).

1.2 The SEL method

The SEL method was first proposed by Pagel et al. (1979). It relies upon the ratio of the sum of the strong forbidden oxygen emission lines with respect to Hβ, the so-called R_{23} ratio: $R_{23} = I([O II]$ $\lambda\lambda 3726, 3729 + [O III] \lambda\lambda 4959, 5007)/I(H\beta)$. Since then many other such ratios have been proposed. The most widely used of these are the calibrations of McGaugh (1991) and Kewley & Dopita (2002), based on detailed photoionization modelling, and the empirical relations provided by Pilyugin (2001a,b), Pilyugin & Thuan (2005) and Pilyugin et al. (2010). Both kinds of calibrations strive to improve the accuracy by making use of the [O III]/[O II] ratio as ionization parameter, which accounts for the large scatter found in the R_{23} versus oxygen abundance calibration, which is larger than observational errors (Kobulnicky, Kennicutt & Pizagno 1999).

Hence, the SEL method is ideally suited to global abundance determinations in distant galaxies, since only the strong lines are visible against the stellar continuum. The abundance scale for ensembles of H II regions in galaxies has recently been calibrated by Dopita et al. (2006a). The basic problem with all ratios of optical forbidden lines to hydrogen RLs is that they are two-valued as a function of chemical abundance. This abundance ambiguity can only be raised by the simultaneous use of several such ratios. An additional problem is that not all SEL methods give similar oxygen abundances: the SEL methods based on calibrations using photoionization models generally tend to overpredict (but not always; see Pérez-Montero et al. 2010; Dors et al. 2011) the observed oxygen abundances derived using the T_e method by 0.2–0.4 dex (Peimbert et al. 2007; Bresolin et al. 2009; López-Sánchez & Esteban 2010; Moustakas et al. 2010). As we should expect, that is not the case for the SEL techniques that are based on calibrations with objects for

which the oxygen abundances are well known from the T_e method. Generally speaking, the SEL method generally returns abundances which are higher than the T_e method, but in better agreement with those derived from RLs of heavy elements (López-Sánchez & Esteban 2010).

1.3 A double-blind test

In this paper, we seek to eliminate some of the systematic errors in abundance determinations by applying the T_e method and the SEL method to theoretically generated H II region spectra, rather than using observed spectra. This has the advantage of eliminating observational errors, but, more importantly, it also provides a direct test of whether the various methods can recover the chemical abundances and physical conditions which were fed into the theoretical models. In order to ensure objectivity, López-Sánchez (who applied the T_e and the SEL methods) was provided with a randomized selection of theoretical H II region models generated by Dopita. The data provided consisted of a set of line fluxes (relative to Hβ) as delivered by the model. The models were identified only by letters, and no information was given about the input physical parameters which were input to generate the models. This is the classical double-blind technique often applied in medicine, but rarely in astrophysics.

In Section 2, we provide details of the techniques used to generate the theoretical spectra; in Section 3 we apply the T_e method to the theoretical spectra and examine how well the input parameters have been recovered. Where possible, we provide correction formulae to apply. Section 4 presents the results provided by the most common SEL techniques. In this section, we also compare the oxygen abundances provided by the SEL methods with the derived T_e and RL abundances in high-quality Galactic and extragalactic H II spectra. Finally, Section 5 gives the conclusions and provides our recommended procedure needed to accurately derive the oxygen abundance in H II regions.

2 THE THEORETICAL MODELS

We have generated a sequence of photoionization models using the MAPPINGS III code, an updated version of the code originally described in Sutherland & Dopita (1993). These models are very similar to those produced by Dopita et al. (2000), and subsequently used by Kewley & Dopita (2002), but the chemical abundances have been specifically modified so as to provide a better fit to the SDSS observed sequence of extragalactic H II regions (Kewley et al. 2006).

Our grid of photoionization models use as stellar input the fluxes computed by the STARBURST 99 code (Leitherer et al. 1999) appropriate for continuous star formation. The input spectrum and the assumed stellar initial mass function input into the STARBURST 99 code are the same as used by Dopita et al. (2000). The later STARBURST 99 models (Vázquez & Leitherer 2005), which incorporate a fully self-consistent mass-loss formulation, were not used as these generate a stellar radiation field that is somewhat too soft relative to these earlier models (see Dopita et al. 2006a, for a detailed discussion of the issue). To summarize, the most likely cause of this discrepancy is probably that the stellar wind is clumpy as a result of radiation pressure instabilities, so a multidimensional model atmosphere would need to be constructed. Effects of stellar rotation can also modify the emergent ionizing spectrum (Levesque, Kewley & Larson 2010). For consistency, we have interpolated the stellar fluxes to match the chemical abundances actually used in the model,

allowing for the abundance scale shift caused by the recalibration of the solar metallicity (Grevesse et al. 2010).

The extragalactic H II region sequence is clearly defined in the observational plane by the standard diagnostic line ratio plots of Baldwin, Phillips & Terlevich (1981) and Veilleux & Osterbrock (1987). These plot the ratios [N II] $\lambda 6584$/Hα, [S II] $\lambda\lambda 6717, 6731$/H$\alpha$ and [O I] $\lambda 6300$/Hα against the [O III] $\lambda 5007$/Hβ emission-line ratio. Kewley et al. (2006) gave these diagnostics for some 45 000 galaxies drawn from the SDSS. Our photoionization models closely reproduce the observational sequence of extragalactic H II regions, bearing in mind that the ionization parameter tends to become higher as the abundance decreases, thanks to the decreasing importance of the ram pressure of the stellar winds (Dopita et al. 2006a).

The solar metallicity for our photoionization models was defined by the solar oxygen abundance given by Grevesse et al. (2010): $12 + \log(O/H) = 8.69 \pm 0.05$. However, the abundances of helium and carbon were assumed to vary according to the formula given by Dopita et al. (2006a). For nitrogen, we use a form similar to that given in Dopita et al. (2006b):

$$12 + \log(N/H) = 7.6 + \log[Z/Z_\odot + (Z/Z_\odot)^2]. \tag{1}$$

Here the zero-point of the nitrogen abundance has been adjusted to prove a better fit in the corresponding Veilleux & Osterbrock (1987) diagnostic diagram. Because nitrogen is an important coolant at high metallicity, this has the incidental effect of improving the fit of the models to the observed extragalactic H II region abundance sequence in the other two diagnostic diagrams. For all models, we include dust and dust physics according to the description in Dopita et al. (2006a), where the depletion factors of the various elements from the gaseous phase are also given.

Our models form a grid in chemical abundance or metallicity, defined by the quantity $12 + \log(O/H)$, and the ionization parameter, $\log q$, the ratio of the number of photons passing per unit area and time to the number density of hydrogen atoms. The q parameter is related to the dimensionless ionization parameter U by $U = q/c$, where c is the speed of light.

Our photoionization models are spherical, with a target ionization parameter for the inner surface. This is unlike the Kewley & Dopita (2002) models, which were plane parallel. Our models are also isobaric with $\log(P/k) = 5.5 \, \mathrm{cm}^{-3} \, \mathrm{K}$, where k is the Boltzmann constant, so that the density varies throughout the model, but is typically 10–$30 \, \mathrm{cm}^{-3}$. Unlike the Kewley & Dopita (2002) models, our models allow for photoelectric heating of the gas by dust grains, and include the effects of radiation pressure, which is becoming appreciable at the higher values of the ionization parameter.

2.1 The double-blind test models

From the theoretical model H II region grid, we have taken, for a fixed metallicity, every second model in $\log q$, and applied to these the standard observational techniques for deriving abundances. In order that no bias was incurred in the analysis, the spectra were randomly selected from the input grid of models, and the raw spectra labelled simply A, B, C, . . . ,Z, AA, . . . ,AG were passed by Dopita to López-Sánchez for analysis. This analysis returned physical conditions, ionization parameters and chemical abundances given by each of the semi-empirical techniques commonly used by observers, which included both the T_e and the SEL methods. We can then compare the results of this analysis to the known inputs into the original models to discover where there exist systematical errors and to evaluate the magnitude of the random errors that can be generated by these techniques. The advantage of this approach is that it

Table 1. The physical and chemical properties of the photoionization models used in the double-blind abundance fitting, organized according to chemical abundance 12+log(O/H), the nominal ionization parameter input into the model, the ionization parameter at the inner surface of the ionized gas, q_{in}, and the mean ionization parameter in the ionized region of the model, $\langle q(H) \rangle$. For each model we give the emission-line weighted mean temperatures (in K) for the [N II], [O III], [S II] and [O II] lines, and the mean recombination temperature for ionized hydrogen, $T(rec)$.

Name	12+log(O/H)	log q	q_{in}	$\langle q(H) \rangle$	$\langle T_{[N II]} \rangle$	$\langle T_{[O III]} \rangle$	$\langle T_{[S II]} \rangle$	$\langle T_{[O II]} \rangle$	$T(rec)$
X	9.39	8.00	5.417E+07	2.598E+07	3363	2987	4277	4284	3439
J	9.39	7.50	2.510E+07	1.171E+07	3041	3620	4201	4194	3908
H	9.39	7.00	1.005E+07	4.426E+06	2881	4282	4352	4357	4307
C	9.39	6.50	3.393E+06	1.376E+06	2617	4568	4494	4558	4403
G	9.17	7.75	5.358E+07	2.432E+07	4478	4619	5544	5487	5004
AA	9.17	7.25	2.140E+07	9.721E+06	4111	5347	5633	5586	5511
O	9.17	6.75	7.393E+07	3.252E+06	3766	5765	5745	5782	5745
I	8.99	8.00	1.212E+08	4.573E+07	5988	5585	6780	6688	5928
R	8.99	7.50	4.210E+07	1.895E+07	6014	6162	6801	6688	6433
AC	8.99	7.00	1.494E+07	6.827E+06	5826	6736	6898	6872	6836
Z	8.99	6.50	4.883E+07	2.119E+06	5351	6936	6865	6935	6902
N	8.69	7.75	1.025E+08	3.850E+07	8604	8069	8782	8713	8294
A	8.69	7.25	3.265E+07	1.460E+07	8680	8448	8751	8729	8618
AG	8.69	6.75	1.076E+07	4.837E+06	8738	8764	8693	8791	8780
U	8.39	8.00	2.720E+08	6.599E+07	10490	10492	10173	10610	10520
F	8.39	7.50	7.609E+07	2.951E+07	10414	10492	10124	10517	10490
W	8.39	7.00	2.314E+07	1.030E+07	10290	10538	10000	10416	10420
AF	8.39	6.50	7.096E+06	3.055E+06	9960	10282	9663	10088	10040
T	8.17	7.75	1.720E+08	4.959E+07	11335	12146	10784	11676	11960
S	8.17	7.25	4.807E+07	1.997E+07	11207	11875	10784	11501	11630
L	8.17	6.75	1.410E+07	6.185E+06	10815	11379	10353	11060	11020
Q	7.99	8.00	3.853E+08	6.985E+07	11843	13584	11123	12474	13250
AE	7.99	7.50	1.005E+08	3.513E+07	11792	13180	11140	12366	12820
AB	7.99	7.00	2.787E+07	1.207E+07	11483	12420	10897	11912	11990
E	7.99	6.50	7.929E+06	3.320E+06	10793	11434	10284	11077	10980
B	7.69	8.25	7.843E+08	8.498E+07	12091	14699	11294	12997	14250
V	7.69	7.75	2.068E+08	5.365E+07	12094	14394	11320	12969	13930
M	7.69	7.25	5.561E+07	2.248E+07	11973	13558	11281	12676	13070
K	7.69	6.75	1.542E+07	6.641E+06	11428	12374	10783	11874	11840
Y	7.39	8.25	8.636E+08	8.379E+07	12220	15354	11398	13299	14830
AD	7.39	7.75	2.191E+08	5.455E+07	12227	14987	11421	13269	14450
P	7.39	7.25	5.769E+08	2.316E+07	12120	13985	11392	12952	13430
D	7.39	6.75	1.575E+08	6.754E+06	11559	12615	10866	12065	12030

totally eliminates errors generated by the observations, and provides spectra of essentially infinite S/N for analysis.

In an ideal world, the parameters returned by the abundance analysis would be the same as those input into the photoionization models. However, in practice the different abundance techniques have different implicit assumptions both about the atomic physics relating to particular ionic species, and more generally, about the physics of the H II region itself. Therefore, we should not expect the results to agree exactly.

The physical and abundance parameters of the input models are given in Table 1. Note that we give three values of the ionization parameter, the nominal ionization parameter input into the model, q, the ionization parameter at the inner surface of the ionized gas, q_{in}, and the mean ionization parameter in the model, $\langle q(H) \rangle$. These are related to each other, but not in any obvious way. For example, q is calculated on the basis of an assumption that the temperature in the inner zone of the H II region is 10 000 K. Because of our isobaric assumption, q_{in} is lower than q for the high-abundance models and higher than q_{in} for the low-abundance models. The ratio of q_{in} to $\langle q(H) \rangle$ is always greater than 2 due to the spherical divergence

of the radiation field, and can reach values as high as 10 where radiation pressure gradients start to play a role in determining the gas pressure.

As stated above, the input stellar spectrum, the physical conditions and the chemical abundance set were chosen so as to replicate, as far as possible, the observed sequence for extragalactic H II regions (Dopita et al. 2000; Kewley et al. 2006). In Fig. 1 we show the two main diagnostic diagrams from Veilleux & Osterbrock (1987) and the diagrams which Dopita et al. (2000) used to separate the chemical abundance from the ionization parameter at the high-abundance end of the scale.

These models display quite a tight relationship between the oxygen abundance, 12+log(O/H), and the electron temperature, T_e, given by the high-ionization zone from the [O III] ($\lambda 4959 + \lambda 5007$)/$\lambda 4363$ ratio, and in the low-ionization ($H^+ + He^0$) zone emitting the [O II] ($\lambda 3726 + \lambda 3729$), [N II] $\lambda 6584$ and [S II] ($\lambda 6717 + \lambda 6731$) lines. This is shown in Fig. 2. Note that there is larger scatter in the plot for the [O III] zone, because the temperature in this zone is more sensitive to the input ionization parameter. On the left-hand plot, the upper left-hand points correspond to
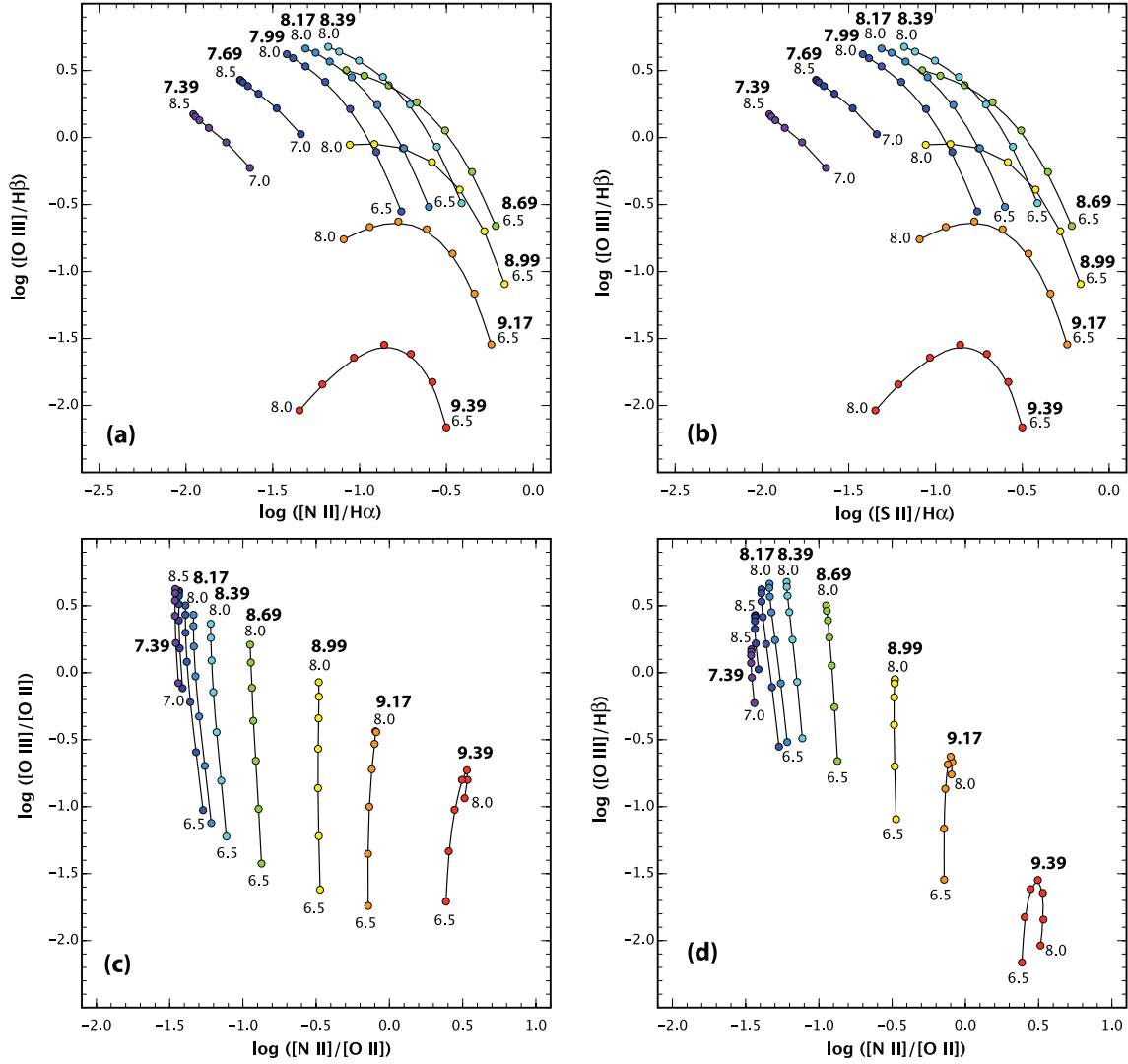
Figure 1. The complete model grid plotted on the Veilleux & Osterbrock (1987) diagnostics, [O III]/Hβ versus [N II]/Hα (panel a) and [O III]/Hβ versus [S II]/Hα (panel b). In the lower panels we show the Dopita et al. (2000) diagnostics [O III]/[O II] versus [N II]/[O II] (panel c) and [O III]/Hβ versus [N II]/[O II] (panel d). The models are identified by their input (gas + dust) $12 + \log{(O/H)}$ (written in bold face and colour coded) and their input ionization parameter, $\log{q}$. Models are stepped by 0.25 dex in $\log{q}$.

high ionization parameter, while the reverse is true for the points in the lower right-hand side of the diagram. There is much less variation in the local ionization parameter in the low-ionization zone of the model H II regions, so that the scatter is less for the right-hand panel of Fig. 2.

For each zone of the model H II region we have generated empirical fits to the oxygen abundance–electron temperature relationship. For [O III], we find

$$T_e[\text{O III}] = 25\,200 - 1400x - 2000|x - 7.0|^{1.7}, \tag{2}$$

while for the low-ionization zone we have

$$T_e(\text{low}) = 9500 + 400x - 2000|x - 6.9|^{2.35}, \tag{3}$$

where $x = 12 + \log{(O/H)}$ in both cases. These curves emphasize once again that the electron temperature is a key diagnostic for chemical abundance in H II regions.

3 APPLICATION OF THE T_e METHOD

3.1 Physical conditions

We have taken care to analyse the model spectra in exactly the same way as an observer would do when presented with the spectrum of real H II regions. If there are no systematic effects in the analysis technique, this exercise should yield the same electron temperatures and chemical abundances as was input into the models. One potential source of difference is the fact that the atomic data used in the nebular models are not necessarily the same as are used in the analysis of the spectra, although in many cases they are. The atomic data used for our models are detailed in Sutherland & Dopita (1993) (see their section 3.5.2), which are similar to the atomic data included in the IRAF task temden in the NEBULAR package by Shaw & Dufour (1995) (see their table 1). The outputs of the various nebular modelling codes have been compared against each other for a number of standard models on more than one occasion through the so-called Lexington Benchmarks code-off exercise (Ferland 1995).
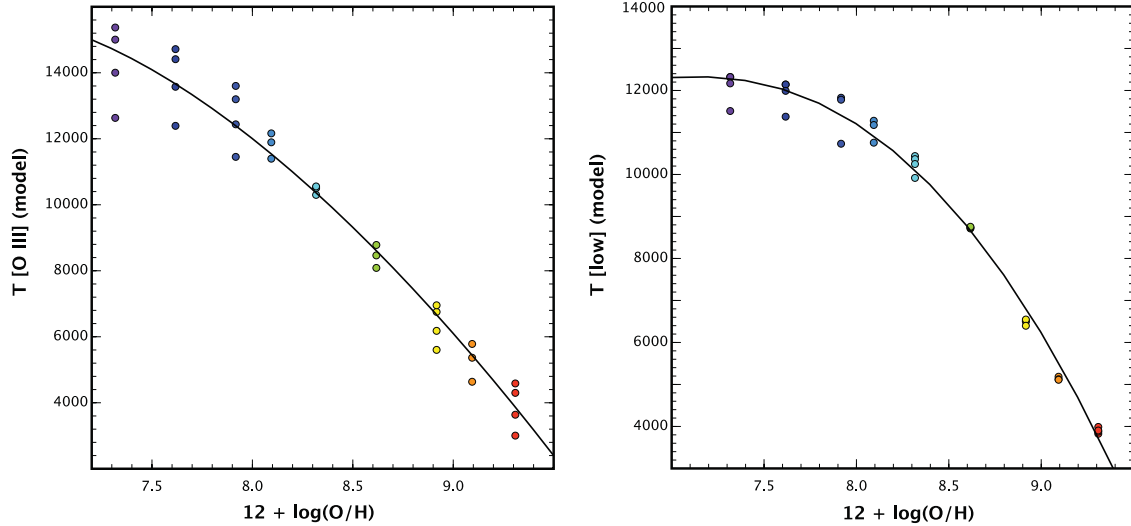
Figure 2. The relation between the oxygen abundance, $12 + \log(O/H)$, and the electron temperature, T_e, given by the models in the high-ionization zone containing [O III] (left) and in the low-ionization zone containing the ions [S II], [O II] and [N II] (right). The empirical fits we have derived for both high- and low-ionization zones as given by equations (2) and (3) are shown as solid lines on these plots.

Any egregious errors made by any one of them have subsequently been eliminated from the appropriate codes. We can therefore be fairly certain that other photoionization codes such as CLOUDY (e.g. Ferland, Fabian & Johnston 1994) will produce very similar output to the MAPPINGS III code used here.

The model spectra were created without considering any extinction or reddening, and not stellar absorption in the H I Balmer lines, to decrease the uncertainties when analysing the data. Thus, for the analysis of the model spectra we have used a reddening coefficient, $c(H\beta)$, and an equivalent width of the stellar absorption underlying the H I Balmer lines, W_{abs}, equal to 0, following López-Sánchez & Esteban (2009).

We derived the electron temperature, T_e, and density, n_e, of the ionized gas of the models using several emission-line ratios. The values obtained for each region are compiled in Table A1. All determinations were computed with the IRAF task temden in the NEBULAR package (Shaw & Dufour 1995). We used the updated atomic data set for the O^+, S^+ and S^{++} ions as input to the NEBULAR routine. The references are indicated in table 4 of García-Rojas et al. (2005).

In accord with Fig. 2, and with equations (2) and (3), we assumed a two-zone approximation for the H II region to describe the temperature structure of the nebulae. In the high-ionization $H^+ + He^+$ zone, we used both the [O III] temperature, T_e[O III], and the mean of T_e[O III], T_e[S III] and T_e[Ar III], T_e(high), as the representative temperature for high ionization potential ions. In the low-ionization zone containing $H^+ + He^0$, we adopted the mean of T_e[O II], T_e[S II] and T_e[N II], T_e(low), for the low ionization potential ion temperatures.

The line ratios used to measure the temperatures are the following:

[O III] $(\lambda 4959 + \lambda 5007)/\lambda 4363$,
[S III] $(\lambda 9069 + \lambda 9530)/\lambda 6311$,
[Ar III] $(\lambda 7135 + \lambda 7751)/\lambda 5192$,
[N II] $(\lambda 6548 + \lambda 6584)/\lambda 5755$,
[O II] $(\lambda 3726 + \lambda 3729)/(\lambda 7319 + \lambda 7330)$ and
[S II] $(\lambda 6717 + \lambda 6731)/(\lambda 4069 + \lambda 4076)$.

We note that some analyses of high-quality, deep spectrophotometric data of bright H II galaxies (e.g. Hägele et al. 2008, 2011;

Pérez-Montero et al. 2010) consider the electron temperature derived for a particular ion only to obtain the ionic abundance of that particular ion. However, the two-zone approximation for the H II region is most widely used in extragalactic analyses.

Since, in the analysis of the spectra, no information about the pressures or density adopted in the models was given, we used the standard density-sensitive line ratios [O II] $\lambda 3726/\lambda 3729$, [N I] $\lambda 5198/\lambda 5200$, [Cl III] $\lambda 5517/\lambda 5537$ and [S II] $\lambda 6717/\lambda 6731$ to derive n_e. In practice, all the models have a common pressure $P/k = 3 \times 10^5$ cm^{-3} K; all density-sensitive ion line ratios should be at their low-density limit. Table A1 compiles the value derived in all cases and the average value adopted for each model. Once n_e was obtained, we used it to derive T_e using the [O III], [S III], [Ar III], [O II], [S II] and [N II] line ratios, and we iterated until convergence was attained.

3.2 Results for T_e

The temperatures derived from the [O III] $(\lambda 4959 + \lambda 5007)/\lambda 4363$ ratio, and the mean temperature derived for the high-ionization species [O III], [S III] and [Ar III], are compared with the [O III] emission-line-weighted temperature given by the model in Fig. 3. The agreement for [O III] is very good, while the mean of the high-ionization species tends to underestimate the true temperature.

We empirically derive the following third-order correction formula to transform the measured [O III] line temperatures into the model [O III] line temperatures:

$$t_4^c = t_4[1 - 0.05(t_4 - 1)^2], \tag{4}$$

where $t_4 = T_e/10\,000$ K is the temperature measured from the spectra and t_4^c is the temperature corrected to that delivered by the corresponding model in units of 10^4 K. The corrections to T_e[O III] are almost always smaller than the intrinsic uncertainty in the derived temperature – typically of the order of 500–1000 K.

For the mean of the high-excitation species [O III], [S III] and [Ar III] the corresponding correction formula is

$$t_4^c = t_4\left(1.12 + 0.02t_4^2\right) - 0.087, \tag{5}$$
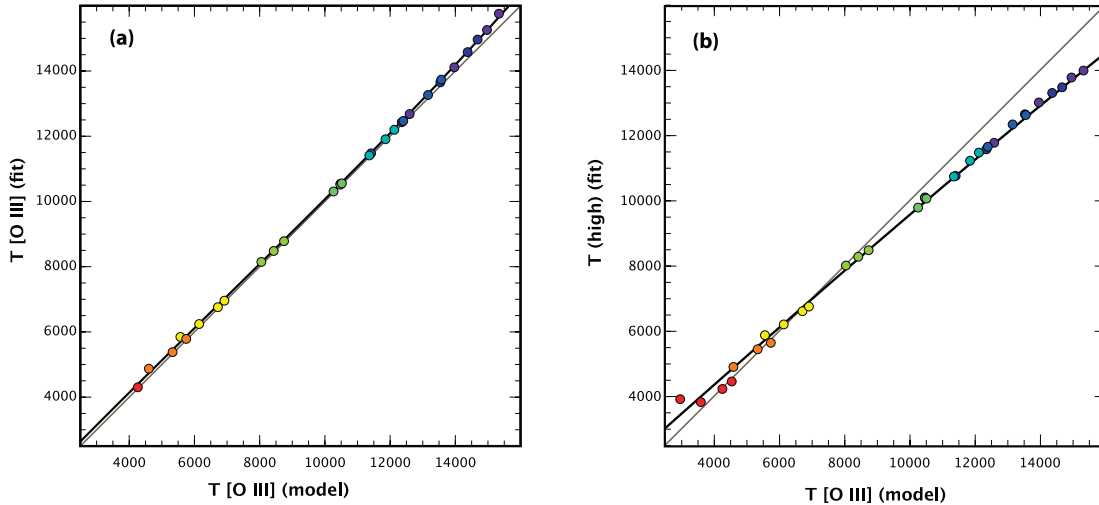
Figure 3. Comparison between the T_e[O III] given by the model (*x*-axis) and the temperature derived by an analysis of the model spectra. The left-hand panel directly compares the [O III] temperature from the model and the derived [O III] temperature, while the right-hand panel compares the fitted temperature drawn from the mean of the [O III], [S III] and [Ar III] temperatures with the [O III] temperature from the model. The empirical fits we have derived are shown as a solid line for both panels. As in Fig. 2, the points are colour coded according to the input abundance set.
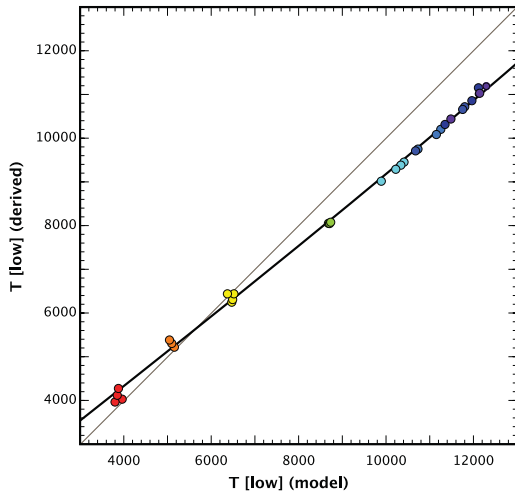
Figure 4. Comparison between the (emission weighted) T_e for the low-ionization species [N II], [O II] and [S II], as returned by the model (*x*-axis) and the T_e derived for these same species from the temperature-sensitive line ratios (*y*-axis). The fit to the data (equation 6) is also plotted.

with t_4 as the average value of the electron temperature derived using the [O III], [S III] and [Ar III] ratios.

For the low-ionization zones of the model H II regions, we use the mean of the [O II], [S II] and [N II] temperatures given by the models, as was also done in the fitting exercise. The result of the comparison is shown in Fig. 4. As we see, we find a clear linear correlation between model and fit, although the slope is not exactly unity. The empirical fit is given by the formula

$$t_4^c = t_4 \left(1.28 - 0.03 t_4^2 \right) - 0.15, \qquad (6)$$

where t_4 and t_4^c are the temperature measured from the spectrum and corrected to that delivered by the corresponding model in units of 10^4 K, respectively. The correlation coefficients of the fits in equations (4), (5) and (6) are all in excess of 0.98.

These differences between the temperatures delivered by the model are the result of the temperature structure within the ionized region. The temperatures delivered by the MAPPINGS III code

are weighted by the emissivity of, for example, the [O III] λ5007 line for [O III]. The [O III] λ4363 line is more strongly affected by temperature stratification as pointed out by Peimbert & Costero (1969), so that the temperature delivered by the measurement of the [O III] (λ4959+λ5007)/λ4363 ratio is different from the strong-line-weighted mean temperature delivered by the code.

For observers who are only able to measure the [O III] temperature in the high-ionization zone (H$^+$ + He$^+$), and need a correction formula to estimate the temperature in the low-ionization (H$^+$ + He^0) zone, the models provide a convenient relationship that fits to an accuracy of ±300 K for temperatures above 10 000 K:

$$T_e(\text{low}) = T_e[\text{O III}] + 450 - 70 \exp \left[(T_e[\text{O III}]/5000)^{1.22} \right]. \qquad (7)$$

Note that the temperature sensitivity to the abundance is strong, and that in high-abundance H II regions, the low-ionization species deliver a lower electron temperature. Note, however, that the form and shape of equation (7) are rather different from that proposed by Garnett (1992), $T_e(\text{low}) = 0.7 \times T_e[\text{O III}] + 3000$. However, both the temperature offset and the slope are similar in the range $8000 \leq T_e[\text{O III}] \leq 12\,000$ where most of the high-quality nebula spectra have been obtained.

3.3 Ionic abundances

The IRAF package NEBULAR (Shaw & Dufour 1995) has been used to analyse the intensities of the forbidden lines using the temperatures and densities derived for the high- and low-ionization zones to derive ionic abundances of O$^+$, O^{++}, N$^+$, S$^+$, S^{++}, Ne^{++}, Ar^{++}, Ar^{+3}, Cl^{++} and Cl^{+3}. The ionic abundances so derived are listed in Appendix A (Table A2).

3.4 Total abundances

In all cases, we adopted O/H = O$^+$/H$^+$ + O^{++}/H$^+$ to determine the total oxygen abundance. Although a very weak nebular He II λ4686 line is produced in several models, the relative contribution of He^{++} to the total amount of helium is negligible, implying that O^{3+} has also a very low abundance in the nebula; thus we did not consider its contribution to the total O/H ratio. For the rest of

Table 2. Total abundances derived from the analysis of line intensity ratios of the model spectra using the IRAF task ionic considering the electron temperature derived from all the high-ionization species, T_e(high), and the low-ionization species, T_e(low), separately. All abundances are expressed in the form of 12+log (X/H) or log (X/O).

Model	O^{++}/O^+	O/H	N/H	N/O	S/H	S/O	Ne/H	Ne/O	Ar/H	Ar/O	Cl/H	Cl/O
A	−0.592	**8.816**	7.432	−1.384	7.147	−1.669	8.374	−0.443	6.883	−1.933	4.424	−4.393
B	0.326	**7.777**	6.129	−1.648	5.974	−1.803	7.109	−0.668	5.512	−2.264	3.426	−4.351
C[a]	−1.771	**8.880**	8.264	−0.616	7.601	−1.279	9.125	0.245	–	–	4.814	−4.066
D	−0.680	**7.571**	5.923	−1.649	5.843	−1.728	7.230	−0.342	5.618	−1.954	3.240	−4.332
E	−1.258	**8.197**	6.629	−1.567	6.466	−1.731	8.165	−0.032	6.632	−1.565	3.761	−4.436
F	−0.126	**8.495**	6.959	−1.536	6.810	−1.686	7.912	−0.583	6.340	−2.155	4.124	−4.371
G	−0.774	**9.157**	8.105	−1.051	7.595	−1.562	8.644	−0.512	7.301	−1.855	4.822	−4.335
H[a]	−0.889	**8.763**	8.205	−0.558	7.669	−1.094	8.600	−0.163	7.441	−1.323	4.884	−3.879
I	−0.654	**9.050**	7.796	−1.254	7.306	−1.744	8.495	−0.555	7.033	−2.017	4.568	−4.482
J[a]	−0.267	**8.560**	8.080	−0.480	7.723	−0.837	8.164	−0.396	7.011	−1.548	4.905	−3.654
K	−0.697	**7.857**	6.235	−1.623	6.142	−1.715	7.530	−0.327	5.931	−1.927	3.444	−4.413
L	−0.925	**8.362**	6.807	−1.555	6.627	−1.735	8.103	−0.259	6.573	−1.789	3.914	−4.448
M	−0.067	**7.805**	6.153	−1.653	6.094	−1.711	7.212	−0.594	5.597	−2.208	3.423	−4.383
N	−0.103	**8.733**	7.332	−1.401	7.116	−1.617	8.160	−0.573	6.630	−2.103	4.411	−4.323
O	−1.863	**9.358**	8.320	−1.038	7.611	−1.747	9.332	−0.026	7.996	−1.362	4.835	−4.523
P	−0.036	**7.502**	5.831	−1.670	5.786	−1.716	6.900	−0.602	5.283	−2.219	3.121	−4.381
Q	0.236	**8.079**	6.456	−1.622	6.308	−1.770	7.422	−0.656	5.829	−2.250	3.721	−4.358
R	−0.647	**9.073**	7.877	−1.196	7.439	−1.633	8.597	−0.476	7.174	−1.899	4.698	−4.374
S	−0.255	**8.302**	6.708	−1.594	6.598	−1.704	7.747	−0.555	6.163	−2.139	3.900	−4.402
T	0.112	**8.256**	6.657	−1.599	6.539	−1.717	7.621	−0.635	6.036	−2.221	3.896	−4.360
U	0.160	**8.456**	6.920	−1.536	6.760	−1.696	7.824	−0.632	6.252	−2.204	4.117	−4.338
V	0.230	**7.780**	6.129	−1.651	6.010	−1.770	7.125	−0.655	5.524	−2.256	3.423	−4.357
W	−0.677	**8.564**	7.055	−1.510	6.847	−1.717	8.167	−0.397	6.634	−1.930	4.132	−4.432
X[a]	−0.567	**8.303**	7.803	−0.501	7.492	−0.811	7.765	−0.538	6.544	−1.759	4.640	−3.663
Y	0.309	**7.486**	5.819	−1.667	5.664	−1.822	6.814	−0.672	5.211	−2.275	3.127	−4.359
Z	−2.018	**9.183**	8.028	−1.155	7.455	−1.728	9.371	0.188	7.939	−1.244	4.695	−4.488
AA	−1.189	**9.320**	8.267	−1.053	7.622	−1.698	8.962	−0.357	7.644	−1.676	4.854	−4.466
AB	−0.447	**8.149**	6.537	−1.612	6.429	−1.720	7.672	−0.477	6.077	−2.072	3.728	−4.422
AC	−1.232	**9.163**	7.988	−1.174	7.449	−1.714	8.923	−0.239	7.563	−1.600	4.699	−4.464
AD	0.243	**7.481**	5.813	−1.668	5.697	−1.784	6.822	−0.660	5.218	−2.264	3.123	−4.358
AE	0.048	**8.092**	6.467	−1.625	6.373	−1.719	7.466	−0.625	5.868	−2.224	3.719	−4.373
AF	−1.473	**8.599**	7.132	−1.467	6.870	−1.729	8.644	0.045	7.177	−1.423	4.151	−4.448
AG	−1.281	**8.873**	7.525	−1.348	7.161	−1.713	8.759	−0.114	7.347	−1.526	4.429	−4.444

[a] For these models, there is no estimation of the high and low electron temperatures using the [O III] and [O II] ions because their auroral lines are not tabulated (see Table A1). Furthermore, the ionic task does not allow electron temperatures lower than 5000 K for the low-ionization ions, so we adopted T_e(low) = 5000 K in these four cases.

the elements, we have to adopt a set of ionization correction factors (ICFs) to correct for the unseen ionization stages. The ICFs adopted here are basically the same as used by López-Sánchez & Esteban (2009).

To derive the nitrogen abundance we assumed the standard ICF by Peimbert & Costero (1969): N/O = N^+/O^+, which is the typical assumption considered in the analysis of the ionized gas in extragalactic H II regions (e.g. López-Sánchez & Esteban 2010).

We measured two ionization stages of sulphur, S^+ and S^{++}, in all spectra. However, a significant contribution of S^{3+} is expected. We adopted the ICF given by Stasińska (1978), which is based on photoionization models of H II regions and is expressed as a function of the O^+/O ratio.

In the case of neon we also applied the classical ICF proposed by Peimbert & Costero (1969), which assumes that the ionization structure of Ne is similar to that of O. This is a good approximation for high-ionization objects, where a small fraction of Ne^+ is expected.

For argon we have determinations of the Ar^{++} and Ar^{3+} abundances. However, some contribution of Ar^+ is expected. Hence,

the total argon abundance was calculated by considering the ICFs proposed by Izotov et al. (1994).

We measured lines Cl^{++} and Cl^{3+}. As can be seen in Table A2, the dominant ionization stage is Cl^{++} and the contribution of Cl^+ to the total abundance is rather small. To take into account the Cl^+ fraction, we have adopted the relation by Peimbert & Torres-Peimbert (1977).

The results we obtain depend on whether we use all of the high-ionization species to determine T_e in the high-ionization zone, T_e(high), and all the low-ionization species to compute T_e in the low-ionization zone, T_e(low), or whether we use only the temperature derived from the [O III] line ratio, T_e[O III]. The total abundances we obtain by these two approaches are shown in Tables 2 and 3, and are shown in graphical form in Figs 5 and 6, respectively.

When all of the high-ionization species are used to derive T_e(high), the oxygen abundance is systematically overestimated by ∼0.2 dex, and the other species seen principally in their high-excitation stages, Ne and Ar, are overestimated by somewhat larger amounts. For 12+log(O/H) = 9.39, the T_e method fails because the IRAF task ionic does not allow electron temperatures lower than 5000 K for the low-ionization ions. If we use only

Table 3. Total abundances derived from the analysis of line intensity ratios of the model spectra using the IRAF task ionic considering only the electron temperature derived from the [O III] lines in the high-ionization zone, T_e[O III], and that derived from the [O II] lines, T_e[O II], in the low-ionization zone. All abundances are expressed in the form of 12+log (X/H) or log (X/O).

Model	O^{++}/O^+	O/H	N/H	N/O	S/H	S/O	Ne/H	Ne/O	Ar/H	Ar/O	Cl/H	Cl/O
A	−0.511	**8.707**	7.362	−1.344	7.114	−1.593	8.269	−0.438	6.797	−1.910	4.388	−4.319
B	0.344	**7.616**	6.021	−1.595	5.884	−1.732	6.968	−0.648	5.406	−2.210	3.337	−4.279
C^a	−1.771	**8.880**	8.264	−0.616	7.601	−1.279	9.125	0.245	–	–	4.814	−4.066
D	−0.662	**7.435**	5.828	−1.607	5.770	−1.666	7.109	−0.327	5.521	−1.915	3.071	−4.365
E	−1.239	**8.065**	6.538	−1.527	6.397	−1.669	8.047	−0.018	6.538	−1.527	3.686	−4.380
F	−0.087	**8.397**	6.896	−1.501	6.759	−1.638	7.823	−0.574	6.271	−2.126	4.076	−4.321
G	−0.559	**9.027**	8.031	−0.996	7.609	−1.418	8.511	−0.515	7.185	−1.842	4.837	−4.190
H^b	−0.934	**8.758**	8.200	−0.558	7.649	−1.109	8.598	−0.160	7.443	−1.315	4.860	−3.898
I	−0.140	**8.888**	7.730	−1.158	7.408	−1.480	8.322	−0.566	6.891	−1.997	4.671	−4.217
J^a	−0.267	**8.560**	8.080	−0.480	7.723	−0.837	8.164	−0.396	7.011	−1.548	4.905	−3.654
K	−0.698	**7.740**	6.153	−1.587	6.073	−1.667	7.427	−0.313	5.849	−1.891	3.371	−4.369
L	−0.903	**8.236**	6.720	−1.516	6.562	−1.674	7.990	−0.247	6.482	−1.755	3.844	−4.392
M	−0.043	**7.675**	6.064	−1.610	6.024	−1.651	7.095	−0.579	5.506	−2.168	3.351	−4.323
N	−0.010	**8.654**	7.291	−1.363	7.100	−1.554	8.084	−0.570	6.575	−2.079	4.388	−4.266
O	−1.759	**9.192**	8.208	−0.984	7.549	−1.643	9.172	−0.020	7.887	−1.305	4.768	−4.424
P	−0.013	**7.367**	5.740	−1.627	5.713	−1.654	6.780	−0.586	5.189	−2.177	3.047	−4.320
Q	0.248	**7.943**	6.364	−1.579	6.232	−1.711	7.303	−0.640	5.737	−2.206	3.645	−4.298
R	−0.508	**8.962**	7.811	−1.151	7.429	−1.533	8.486	−0.476	7.080	−1.882	4.686	−4.276
S	−0.228	**8.185**	6.629	−1.556	6.538	−1.647	7.642	−0.543	6.080	−2.105	3.837	−4.348
T	0.139	**8.143**	6.583	−1.560	6.480	−1.663	7.520	−0.623	5.958	−2.185	3.835	−4.308
U	0.198	**8.363**	6.862	−1.501	6.717	−1.646	7.740	−0.623	6.189	−2.174	4.071	−4.292
V	0.243	**7.639**	6.033	−1.606	5.930	−1.709	7.001	−0.638	5.428	−2.210	3.344	−4.294
W	−0.645	**8.451**	6.977	−1.473	6.793	−1.658	8.063	−0.388	6.550	−1.901	4.074	−4.377
X^a	−0.567	**8.303**	7.803	−0.501	7.492	−0.811	7.765	−0.538	6.544	−1.759	4.640	−3.663
Y	0.297	**7.319**	5.701	−1.619	5.562	−1.757	6.670	−0.650	5.098	−2.221	3.031	−4.289
Z	−1.929	**9.027**	7.922	−1.105	7.393	−1.634	9.222	0.195	7.844	−1.183	4.626	−4.400
AA	−1.054	**9.173**	8.172	−1.002	7.591	−1.583	8.818	−0.356	7.522	−1.651	4.821	−4.352
AB	−0.425	**8.022**	6.450	−1.572	6.362	−1.660	7.558	−0.464	5.986	−2.036	3.657	−4.365
AC	−1.134	**9.022**	7.895	−1.127	7.406	−1.616	8.787	−0.235	7.450	−1.571	4.652	−4.370
AD	0.251	**7.330**	5.709	−1.621	5.610	−1.720	6.690	−0.641	5.116	−2.215	3.037	−4.293
AE	0.071	**7.967**	6.383	−1.584	6.306	−1.661	7.355	−0.611	5.781	−2.185	3.650	−4.316
AF	−1.445	**8.476**	7.046	−1.429	6.809	−1.667	8.531	0.056	7.088	−1.388	4.083	−4.392
AG	−1.214	**8.740**	7.434	−1.305	7.109	−1.630	8.633	−0.106	7.244	−1.495	4.373	−4.367

[a] For these models there is no estimation of the high and low electron temperatures using the [O III] and [O II] ions because their auroral lines are not tabulated (see Table A1). The results shown here are the same as those in Table 2 because we used T_e(high) and T_e(low). Furthermore, the ionic task does not allow electron temperatures lower than 5000 K for the low-ionization ions, so we adopted T_e(low) = 5000 K in these four cases.

the temperature derived from the [O III] lines, T_e[O III], using the [O III] ($\lambda4959+\lambda5007$)/$\lambda4363$ ratio in the high-ionization zone, and the temperature derived from the [O II] lines, T_e[O II], using the [O II] ($\lambda3726+\lambda3729$)/($\lambda7319+\lambda7330$) ratio in the low-ionization zone, the systematic error is much less, especially for the total oxygen abundance, although it is still slightly over-predicted.

Although there are small systematic errors in this procedure, all are correctable. It is clear that the T_e method returns reliable abundances. Provided that the [O III] ($\lambda4959+\lambda5007$)/$\lambda4363$ ratio is used to determine the T_e in the high-ionization zone, the scatter in the derived abundances of O, N, S and Cl is typically ±0.1 dex, provided that the O abundance is below 12+log(O/H) < 9. For high abundances, the T_e method returns systematically low abundances, where it can be applied. This is in agreement with the work of Stasińska (2002, 2005), who predicted that temperature gradients in these high-metallicity H II regions can cause the abundances to be underestimated by as much as ∼0.4 dex.

For both Ne and Ar the systemic error and the scatter are distressingly large. We do not think that this is a consequence of using slightly different atomic data for models and line analysis using IRAF.

However, the cause is likely to be different in the two cases. In the case of Ne, the error is probably caused by the fact that only Ne^{++} is observable, and the [Ne III] $\lambda\lambda3869$, 3968 has sufficiently high excitation energy that the line emissivity is strongly biased towards the hottest part of the H II region. In the case of Ar, charge-exchange processes are very important in determining the ionic balance, and these strongly affect the ionization balance and therefore the ICFs (Dopita et al. 1997). Furthermore, the assumptions of the ICFs used to derived the total abundances of Ne and Ar from their ionic abundances may be not valid in some cases (e.g. Pérez-Montero et al. 2007).

Given that Fig. 2 shows that the electron temperature and the abundance are closely correlated, it is interesting to see just how well the oxygen abundance can be recovered from the measured [O III] temperature alone. To do this, we used our empirical relation (equation 4) to correct the measured temperature and then applied the relationship between T_e[O III] and 12+log(O/H) given by equation (2) to obtain the oxygen abundance. The result is shown in Fig. 7. For abundances 12+log(O/H) > 8.0, the abundances are recovered to an accuracy of ±0.1 dex. At lower abundances, significant scatter is introduced by variations in the ionization parameter
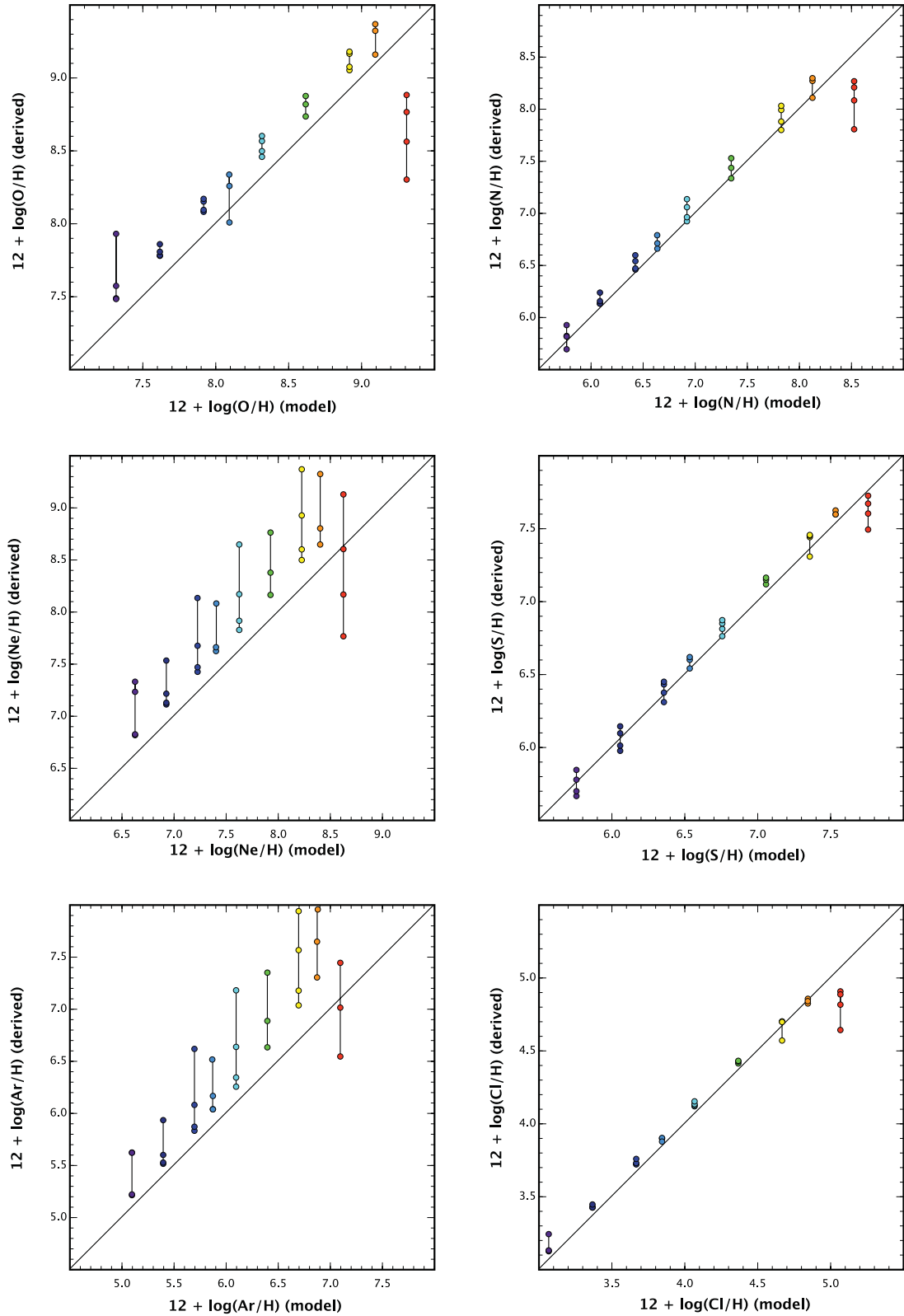
Figure 5. A comparison of the total abundances derived from the analysis of line intensity ratios of the model spectra and using T_e(high) and T_e(low) as representative for the electron temperature of the high- and low-ionization species, respectively (see Table 2), with the total abundances provided by the models. The fit is fairly good for the species for which the optical line emission arises principally in the low-ionization zone, N, S and Cl, but there is clearly a systematic error for the other species, O, Ne and Ar. For 12+log(O/H) = 9.39, the T_e method fails because the IRAF task ionic does not allow electron temperatures lower than 5000 K for the low-ionization ions, and hence T_e(low) = 5000 K was adopted.
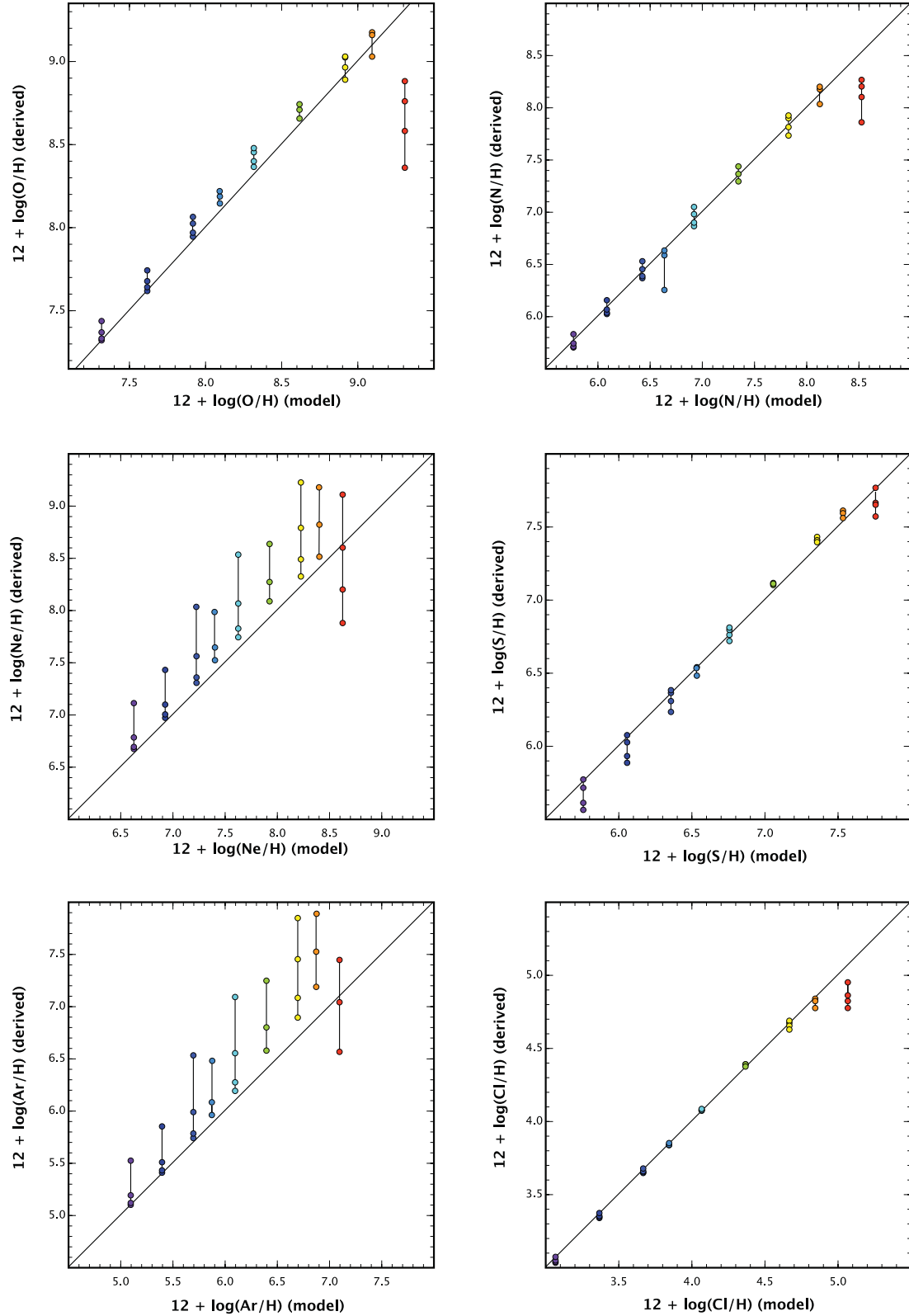
Figure 6. A comparison of the total abundances derived by using T_e[O III] using the [O III] (λ4959+λ5007)/λ4363 ratio in the high-ionization zone and T_e[O II] using the [O II] (λ3726+λ3729)/(λ7319+λ7330) ratio in the low-ionization zone (see Table 3) with the total abundances provided by the models. As in Fig. 5, the fit is fairly good for the species for which the optical line emission arises principally in the low-ionization zone, N, S and Cl. Although it is slightly overpredicting the model abundances, the fit is now acceptable for O, except for 12+log(O/H) = 9.39 because of the aforementioned problem when calculating T_e[O II] for the low-ionization ions. However, our fits still have a systematic error in the case of Ne (which is seen only in its high-ionization stage Ne^{++}) and Ar (for which the emission is also dominated by its high-ionization lines, and which is strongly affected by charge-exchange reactions). Random errors are also larger for these species.
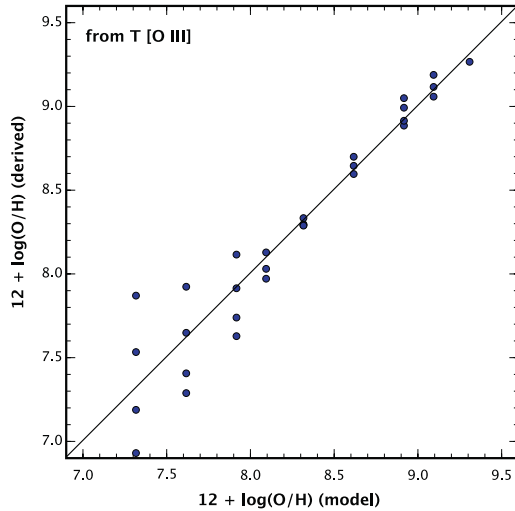
Figure 7. A comparison of the abundances derived by using only T_e[O ɪɪɪ] measured from the [O ɪɪɪ] ($\lambda4959+\lambda5007$)/$\lambda4363$ ratio. For abundances 12+log(O/H) >8.0, the abundances are recovered to an accuracy of ±0.1 dex. At lower abundances, the scatter is much increased because of the increased sensitivity of T_e[O ɪɪɪ] with the ionization parameter in this region.

q, and it becomes essential to determine this parameter independently.

4 APPLICATION OF THE SEL METHOD

The SEL technique to derive nebular abundances is typically used when the spectra are of too low S/N for the temperature-sensitive emission lines to be detectable. This typically encompasses the majority of the global determinations of metallicity in external galaxies, and all galaxies with redshifts large enough to be of cosmological interest. An extensive review of 10 metallicity calibrations, including theoretical and empirical methods, has been presented by Kewley & Ellison (2008), using data gathered from the SDSS. López-Sánchez & Esteban (2010) also review the most common empirical calibrations and compare their results with those derived using the T_e method. The majority of the empirical calibrations rely on ratios between bright emission lines to estimate the oxygen abundance. The most commonly used of these are known by their shorthand contractions: R_{23}, S_{23}, P, N_2, O_3N_2, N_2O_2 and y. Their definitions are

$$R_3 = \frac{I([\text{O ɪɪɪ}])\lambda4959 + I([\text{O ɪɪɪ}])\lambda5007}{\text{H}\beta}, \tag{8}$$

$$R_2 = \frac{I([\text{O ɪɪ}])\lambda\lambda3726, 3729}{\text{H}\beta}, \tag{9}$$

$$R_{23} = R_3 + R_2, \tag{10}$$

$$P = \frac{R_3}{R_{23}}, \tag{11}$$

$$y = \log\frac{R_3}{R_2} = \log\frac{1}{P^{-1} - 1}, \tag{12}$$

$$N_2 = \log\left(\frac{I([\text{N ɪɪ}])\lambda6584}{\text{H}\alpha}\right), \tag{13}$$

$$O_3N_2 = \log\left\{\frac{(I([\text{O ɪɪɪ}])\lambda5007/\text{H}\beta)}{(I([\text{N ɪɪ}])\lambda6584/\text{H}\alpha)}\right\}, \tag{14}$$

$$N_2O_2 = \log\left(\frac{I([\text{N ɪɪ}])\lambda6584}{I([\text{O ɪɪ}])\lambda\lambda3726, 3729}\right), \tag{15}$$

$$S_{23} = \frac{I([\text{S ɪɪ}])\lambda\lambda6717, 6731 + I([\text{S ɪɪɪ}])\lambda\lambda9076, 9532}{\text{H}\beta}, \tag{16}$$

$$S_{23}O_{23} = \frac{S_{23}}{R_{23}}. \tag{17}$$

Simple line ratios such as R_{23} (Jensen, Strom & Strom 1976; Pagel et al. 1979), S_{23} (Vílchez & Esteban 1996; Christensen, Petersen & Gammelgaard 1997; Díaz & Pérez-Montero 2000) – or indeed any forbidden line to RL ratio – suffer from being two-valued, and hence a separate calibration for the low- and high-metallicity regimes is usually needed. In the case of the R_{23} index, the calibrations are given for 12+log(O/H) $\lesssim$ 8.1 (low metallicity) and 12+log(O/H) $\gtrsim$ 8.4 (high metallicity). That means that a very large fraction of the star-forming regions lie in the ill-defined turning zone around 12+log(O/H) $\sim$ 8.20–8.30, where regions with the same R_{23} value have oxygen abundances that differ by almost an order of magnitude (see e.g. fig. A.1 in López-Sánchez & Esteban 2010). The reason for this behaviour is that the intensity of the oxygen (or any other heavy element) lines does not monotonically increase with metallicity. At low abundance, the lines of the heavy element being considered are weak relative to a hydrogen RL due to their low abundance. However, at high abundance they are weak due to the low electron temperature, which suppresses collisional excitations into the excited state responsible for the forbidden line. The turnaround in the line ratio can be extended to higher abundance by choosing lines with lower excitation potentials which make the ratio less temperature sensitive, hence the utility of S_{23} over R_{23}. The use of multiple line ratios also helps to remove the abundance ambiguities.

Ratios such as O_3N_2 (Alloin et al. 1979; Pettini & Pagel 2004) were introduced in an attempt to sidestep the abundance ambiguity entirely. This ratio is much more monotonic in abundance because of the strong secondary component of N enrichment alluded to above (see equation 1). This helps at high abundance, but the ratio once again becomes ambiguous when 12+log(O/H) $\lesssim$ 8.0. A ratio such as N_2O_2 (Dopita et al. 2000; Kewley & Dopita 2002) also provides a useful calibration for metallicity at high abundance. Its advantage is that both N^+ and O^+ coexist in the same zone of the nebula, the [O ɪɪɪ] lines become weaker at high metallicity due to the low electron temperature, while the [N ɪɪ] lines become stronger due to the higher relative abundance of this element. However, its disadvantage is that the nitrogen and oxygen emission lines are widely separated in wavelength, making flux calibration and reddening corrections more critical.

The fundamental weakness in the use of all these strong-line ratios is that the overall spectrum of an H ɪɪ region depends not only upon the chemical abundances, but also upon the ionization parameter q or U. That this is so is abundantly obvious from Fig. 1. The importance of this was recognized by Baldwin et al. (1981), who were amongst the first to use line ratio diagnostic diagrams. However, the first empirical calibration involving an ionization parameter was presented by McGaugh (1991), who developed models of H ɪɪ regions using the photoionization code CLOUDY. McGaugh (1991) introduced the y parameter to derive (together with the R_{23} ratio) the oxygen abundance using only the bright oxygen lines. The

analytical expressions for these models were given by Kobulnicky et al. (1999).

It is clear from Fig. 1(c), and as emphasized by Dopita et al. (2000) and Kewley & Dopita (2002), that the [O III]/[O II] ratio is probably the best one to use to determine the ionization parameter, particularly if the [N II]/[O II] ratio is also measured. To a lesser extent R_3 can also be used. Kewley & Dopita (2002) provided a procedure to allow a simultaneous solution of both $\log q$ and $12+\log(O/H)$, which involves the y and R_{23} parameters, although they also give a parametrization of the oxygen abundance and $\log q$ using other parameters such as [S III]/[S II] (which is also a good estimator of the ionization parameter), N_2O_2, N_2, S_{23} and O_3N_2. Later, Kobulnicky & Kewley (2004) provided a parametrization of the Kewley & Dopita (2002) method using the y and R_{23} parameters with a form similar to that given by the McGaugh (1991) calibration. Following this method, $\log q$ and the oxygen abundance are computed iteratively using only the bright oxygen lines.

Pilyugin and his co-workers have attempted an empirical calibration of the R_{23} and P parameters using the bright [O III] $\lambda\lambda4959$, 5007 and [O II] $\lambda\lambda3726$, 3729 nebular lines. To get this calibration, they used a combination of photoionization models and empirical data from observed H II regions where the auroral [O III] $\lambda4363$ line was available. Indeed, the so-called Pilyugin parameter, P, was introduced by Pilyugin (2000), after confirming that the R_{23} parameter has a systematic error depending on the hardness of the ionizing radiation. Hence, the excitation parameter P also considers the ionization degree of the H II region. His first empirical calibrations involving both the R_{23} and the P parameter were presented in Pilyugin (2001a) and Pilyugin (2001b) for high- and low-metallicity H II regions. Subsequently, Pilyugin & Thuan (2005) and Pilyugin et al. (2010) tried to improve such calibrations including more spectroscopic measurements of H II regions in spiral and irregular galaxies derived using the T_e method. Finally, Pilyugin & Mattsson (2011) provided another empirical calibration considering only the R_3, N_2 and S_2 parameters (the so-called NS calibration), which was derived to estimate oxygen abundances in galaxies whose spectrum is lacking the [O II] $\lambda\lambda3726$, 3729 emission lines.

4.1 Comparison of the SEL techniques

We have applied all of these commonly used SEL techniques to our model spectra to derive oxygen abundances, again via a double-blind procedure. The different SEL techniques fall into various classes, depending on which combination of strong-line ratios are used. Table A3 lists the values of all these parameters derived for each model. This table also includes the value derived for the q parameter obtained from the optimal calibration provided by Kewley & Dopita (2002) and Kobulnicky & Kewley (2004). Table 4 compiles the oxygen abundances derived for each model, indicating which branch (high- or low-metallicity) the model spectra would fall into when using the R_{23} parameter. We considered the values of the oxygen abundances derived from the T_e method to choose the expressions of the lower or the upper branch provided by the empirical calibrations. For models F, U, W and AF, for which we obtained oxygen abundances of $12+\log(O/H) \sim 8.4$ using the T_e method, the results provided by both the low- and high-metallicity branches are tabulated, and both sets of data are plotted in Figs 8–11. Note that the calibrations that invoke the N_2, O_3N_2, S_{23} or $S_{23}O_{23}$ parameters give the same result for the low- and high-metallicity branches. The Kewley & Dopita (2002) calibration using the N_2O_2 parameter is only valid for objects in the high-metallicity branch.

To quantify the goodness of these SEL techniques, we have performed a linear fit between the oxygen abundances derived from these empirical methods and the oxygen abundances assumed by the models. In all cases, for models with $12+\log(O/H) = 8.39$ we have assumed the average value between the high- and low-metallicity branches. We note that not all the models have been considered in this fit, but only those within the validity range of each SEL calibration. Table 5 compiles the results for these linear fits, including the correlation coefficient, the dispersion of the data and the average value of the difference between the abundance given by the SEL method and that assumed by the models (offset). The first row of Table 5 lists the results of a linear fit between the oxygen abundances derived following the T_e method and those imposed by the models. This fit does not consider the models with $12+\log(O/H) = 9.39$ (see Fig. 6).

4.1.1 N_2 and O_3N_2 methods

Let us first consider the techniques which rely upon the N_2 parameter: that of Denicoló et al. (2002) and those drawn from Pettini & Pagel (2004) which involve a linear interpolation of the N_2 parameter, a cubic fit to this same parameter and their fit using the O_3N_2 parameter. These are shown in Fig. 8. All these calibrations have a similar scatter $\sim$0.20–0.25 dex. However, they are well behaved (if rather curved) in their abundance sequence. This type of curvature was also observed by Kewley & Ellison (2008), if we can interpret the mass sequence of galaxies as equivalent to an abundance sequence.

Yin et al. (2007) indicated that the N_2 and the O_3N_2 indices are only useful for calibrating metallicities of galaxies with $12+\log(O/H) < 8.5$, while Pérez-Montero & Contini (2009) established that empirical calibrations using the O_3N_2 parameter are not valid for objects with $12+\log(O/H) \lesssim 8.0$. Following Fig. 8, we suggest that the N_2 method should not be applied for $12+\log(O/H) \gtrsim 8.7$–9.0, while the O_3N_2 calibration provided by Pettini & Pagel (2004) is only valid for $12+\log(O/H) \gtrsim 8.7$. Importantly, in all cases the result has a high uncertainty, $\sim$0.25 dex, which is a consequence of the lack of any parameter which considers the ionization degree of the gas. Furthermore, in the case of galaxies showing an overabundance of nitrogen (e.g. Pustilnik et al. 2004; López-Sánchez et al. 2007; López-Sánchez & Esteban 2010; Monreal-Ibero et al. 2010), the application of any N_2 or O_3N_2 calibration will provide misleading oxygen abundances.

4.1.2 S_{23} and $S_{23}O_{23}$ methods

Fig. 9 compares the oxygen abundances assumed by our models with the results provided using the Pérez-Montero & Díaz (2005) calibrations, which consider the S_{23} and $S_{23}O_{23}$ parameters. In the case of using the S_{23} index, the calibration seems to be valid up to $12+\log(O/H) \sim 9.0$, having a dispersion of 0.24 dex. However, this method cannot be applied for $12+\log(O/H) \gtrsim 9.0$. On the other hand, the $S_{23}O_{23}$ calibration works quite well at high metallicities, $12+\log(O/H) \gtrsim 8.5$. But it is not valid for $12+\log(O/H) \lesssim 8.2$ as the result basically does not depend on metallicity, having a constant value which depends on q, and a high dispersion, >0.6 dex.

Much of the scatter in the Denicoló et al. (2002), Pettini & Pagel (2004) and Pérez-Montero & Díaz (2005) calibrations is due to a failure to include the effects of the ionization parameter on the line ratios. This is especially important in the analysis of 2D spectroscopic data, as the oxygen abundance maps derived using these calibrations may directly reflect the ionization structure of the H II

Table 4. Results for the oxygen abundance, in the form $12+\log(O/H)$, according to the most commonly used empirical SEL calibrations.

Model	T_e	Branch	M91	KD02o	KK04	KN2O2	P01	PT05	PVT10	PM11	D02	PP04a	PP04b	PP04c	S_{23}	$S_{23}O_{23}$
A	8.71	High	8.53	8.84	8.67	8.64	8.21	8.11	8.44	8.49	8.56	8.46	8.41	8.40	8.96	8.60
B	7.62	Low	7.50	7.67	7.81	–	7.39	7.36	7.17	7.12	7.62	7.73	7.74	7.94	7.45	7.74
C	8.88	High	9.13	9.31	9.35	9.24	8.86	8.43	9.11	8.94	8.72	8.59	8.58	9.25	8.53	9.65
D	7.44	Low	7.23	7.57	7.53	–	7.34	7.01	6.73	6.31	7.71	7.80	7.84	8.28	7.28	8.31
E	8.01	Low	7.96	7.85	8.10	–	8.77	6.94	7.18	6.74	8.21	8.19	8.18	8.51	8.17	8.50
Fl[a]	8.40	Low	8.17	8.28	8.36	–	8.02	8.13	7.93	7.95	8.26	8.23	8.20	8.17	8.74	8.37
Fu[a]	8.40	High	8.17	8.73	8.55	8.34	8.27	8.22	7.93	7.95	8.26	8.23	8.20	8.17	8.74	8.37
G	9.03	High	9.07	9.22	9.16	9.09	8.84	8.70	8.73	8.76	8.54	8.45	8.39	8.69	8.46	9.30
H	8.76	High	9.14	9.33	9.35	9.26	8.88	8.57	8.94	8.88	8.66	8.54	8.51	9.05	8.39	9.67
I	8.89	High	8.95	9.02	9.06	8.92	8.76	8.69	8.65	8.67	8.44	8.37	8.31	8.45	8.55	8.94
J	8.56	High	9.22	9.37	9.47	9.28	8.91	8.69	9.01	9.00	8.49	8.41	8.35	8.98	8.04	9.74
K	7.74	Low	7.54	7.81	7.79	–	7.78	7.15	7.15	6.74	7.94	7.98	8.03	8.31	7.67	8.33
L	8.24	Low	8.12	7.97	8.27	–	8.57	7.52	7.67	7.28	8.32	8.28	8.24	8.41	8.42	8.42
M	7.68	Low	7.50	7.58	7.80	–	7.40	7.41	7.18	7.07	7.78	7.85	7.91	8.07	7.62	8.07
N	8.65	High	8.61	8.77	8.74	8.63	8.41	8.36	8.52	8.55	8.38	8.32	8.27	8.26	8.74	8.51
O	9.19	High	9.00	9.07	9.14	9.06	8.65	8.29	8.76	8.67	8.81	8.65	8.70	8.97	9.02	9.29
P	7.37	Low	7.16	7.53	7.52	–	7.00	7.20	6.75	6.62	7.54	7.67	7.64	8.05	7.24	8.04
Q	7.94	Low	7.91	7.98	8.15	–	7.73	7.74	7.53	7.52	7.86	7.92	7.98	7.98	7.90	7.86
R	8.96	High	8.88	8.97	9.02	8.92	8.61	8.51	8.56	8.57	8.61	8.51	8.46	8.54	8.86	8.96
S	8.19	Low	8.07	8.13	8.27	–	8.00	7.98	7.77	7.64	8.17	8.16	8.16	8.17	8.34	8.22
T	8.14	Low	8.05	8.08	8.26	–	7.85	7.92	7.67	7.68	8.02	8.04	8.08	8.05	8.20	8.04
Ul[a]	8.36	Low	8.13	8.22	8.32	–	7.90	8.02	7.88	7.89	8.13	8.12	8.13	8.08	8.40	8.13
Uu[a]	8.36	High	8.13	8.58	8.54	8.33	8.34	8.29	7.88	7.89	8.13	8.12	8.13	8.08	8.40	8.13
V	7.64	Low	7.50	7.65	7.81	–	7.38	7.36	7.16	7.11	7.65	7.75	7.78	7.97	7.51	7.83
Wl[a]	8.45	Low	8.27	8.29	8.41	–	8.45	8.04	7.99	8.00	8.43	8.36	8.31	8.35	8.72	8.42
Wu[a]	8.45	High	8.27	8.78	8.59	8.38	8.11	7.99	7.99	8.00	8.43	8.36	8.31	8.35	8.72	8.42
X	8.30	High	9.32	9.40	–	9.28	8.92	8.62	9.12	9.18	8.36	8.31	8.26	9.05	7.71	9.76
Y	7.32	Low	7.15	7.47	7.52	–	7.01	7.13	6.76	6.68	7.39	7.55	7.38	7.92	7.12	7.70
Z	9.03	High	8.76	9.01	8.98	8.92	8.36	7.98	8.73	8.61	8.82	8.66	8.72	8.95	9.29	9.08
AA	9.17	High	9.03	9.17	9.14	9.07	8.73	8.52	8.66	8.65	8.71	8.58	8.57	8.77	8.81	9.28
AB	8.02	Low	7.90	7.84	8.12	–	7.96	7.69	7.61	7.36	8.11	8.11	8.13	8.22	8.12	8.25
AC	9.02	High	8.79	9.02	8.97	8.92	8.42	8.18	8.53	8.53	8.77	8.63	8.65	8.70	9.12	9.00
AD	7.33	Low	7.14	7.46	7.52	–	6.99	7.14	6.75	6.66	7.42	7.57	7.43	7.94	7.15	7.79
AE	7.97	Low	7.90	7.89	8.14	–	7.75	7.76	7.55	7.51	7.94	7.98	8.03	8.05	8.02	8.02
AFl[a]	8.48	Low	8.38	7.85	8.44	–	9.43	7.29	7.80	7.93	8.51	8.42	8.37	8.62	8.84	8.61
AFu[a]	8.48	High	8.38	8.80	8.72	8.47	8.07	7.75	7.80	7.93	8.51	8.42	8.37	8.62	8.84	8.61
AG	8.74	High	8.45	8.76	8.65	8.67	8.03	7.74	8.48	8.50	8.69	8.56	8.54	8.62	9.15	8.71

[a] For these models, for which we derived $12+\log(O/H) \sim 8.4$ following the T_e method, we list the results of the empirical calibrations considering both the low- and the high-metallicity branches.

Note. The empirical calibrations and the parameters used for each of them are the following:

M91 – McGaugh (1991) using R_{23} and y; KD02 – Kewley & Dopita (2002) using R_{23} and the ionization parameter defined in that paper, q_{KD02o}; KK04 – Kobulnicky & Kewley (2004) using R_{23} and the ionization parameter defined in that paper, q_{KK04}; KN2O2 – Kewley & Dopita (2002) using the N_2O_2 parameter (calibration only valid for objects in the high-metallicity branch); P01 – Pilyugin (2001a,b) using R_{23} and P; PT05 – Pilyugin & Thuan (2005) using R_{23} and P; PVT10 – Pilyugin et al. (2010) using R_{23}, P, N_2 and S_2; PM11 – Pilyugin & Mattsson (2011) using R_3, N_2 and S_2; D02 – Denicoló, Terlevich & Terlevich (2002) using the N_2 parameter; PP04a – Pettini & Pagel (2004) using a linear fit to the N_2 parameter; PP04b – Pettini & Pagel (2004) using a cubic fit to the N_2 parameter; PP04c – Pettini & Pagel (2004) using the O_3N_2 parameter; S_{23} – Pérez-Montero & Díaz (2005) using S_{23}; $S_{23}O_{23}$ – Pérez-Montero & Díaz (2005) using S_{23} and R_{23}.

region and not the actual changes in metallicity (López-Sánchez et al. 2011). It is clear that the scatter could be reduced to ~0.1 dex if the ionization parameter is taken into account, since the vertical separation of the points on the figures is almost entirely the result of the different ionization parameters used in the models. However, this would not solve the curvature issue.

4.1.3 Pilyugin method

We next consider the Pilyugin et al. empirical calibrations of R_{23} and P (Pilyugin 2001a,b; Pilyugin & Thuan 2005; Pilyugin et al. 2010; Pilyugin & Mattsson 2011). As we discussed before, P is an empirical parameter that traces the ionization degree of the H II region.

The results we obtain are shown in Fig. 10. The main characteristic of these SEL calibrations is that there is a systematic offset in the sense that the Pilyugin method tends to underestimate the abundance by up to ~0.25 dex (Pilyugin 2001a,b), ~0.4 dex (Pilyugin et al. 2010) and ~0.5 dex (Pilyugin & Thuan 2005; Pilyugin & Mattsson 2011). It is also clear that the scatter for the Pilyugin (2001a,b) and Pilyugin & Thuan (2005) empirical calibrations is typically 0.3 dex. In both calibrations, the scatter becomes considerably larger in the $12+\log(O/H) \sim 8.0$–8.4 range, as a result of the ambiguity in determining the appropriate branch on which R_{23} is located. We note that for this intermediate-metallicity regime, it is common to give an average value between the oxygen abundances derived for the high- and low-metallicity branches if the Pilyugin (2001a,b) and
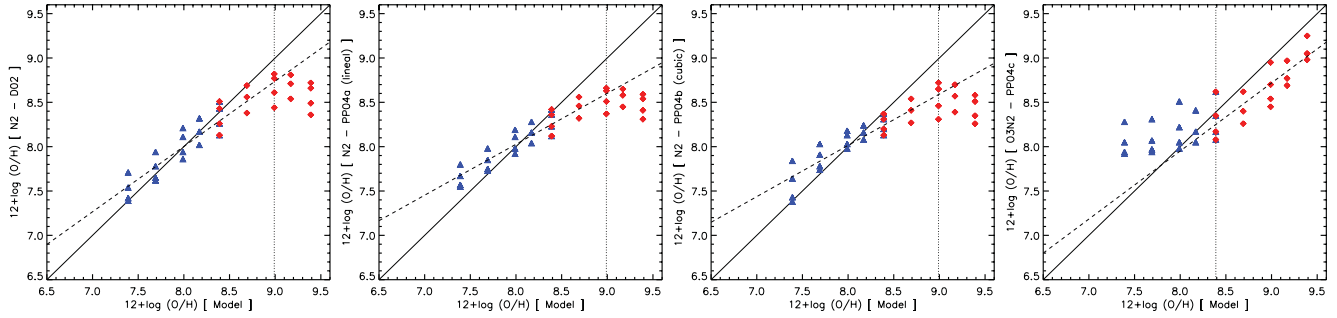
Figure 8. Comparison between the total abundances used for the models (*x*-axis) and those computed using the empirical calibrations considering the N_2 and the O_3N_2 parameters from Denicoló, Terlevich & Terlevich (2002) and Pettini & Pagel (2004). The continuous line represents $y = x$. Red diamonds and blue triangles represent high- and low-metallicity models, respectively. The vertical dotted line indicates the lower (when using the N_2 parameter) or upper (when using the O_3N_2 parameter) limit of validity of the fits. The dashed line indicates the fit to the data within the appropriate metallicity range.
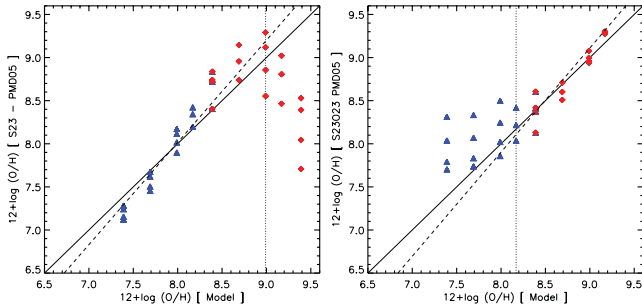
Figure 9. Comparison between the total abundances used for the models (*x*-axis) and those computed using the empirical calibrations considering the S_{23} and the $S_{23}O_{23}$ parameters from Pérez-Montero & Díaz (2005). The continuous line represents $y = x$. Red diamonds and blue triangles represent high- and low-metallicity models, respectively. The vertical dotted line indicates the upper (using the S_{23} parameter) or lower (using the $S_{23}O_{23}$ parameter) limit of the validity of the fits. The dashed line indicates the fit to the data within the appropriate metallicity range.

Pilyugin & Thuan (2005) methods are used (e.g. López-Sánchez & Esteban 2010; Moustakas et al. 2010).

In the case of the Pilyugin et al. (2010) and Pilyugin & Matts-son (2011) methods (which also consider the N_2 and S_2 indices), three calibrations are provided for low, intermediate and high metallicities. In these cases, the scatter is slightly lower, ∼0.14 and ∼0.25 dex, respectively, than the scatter found using the previ-

ous calibrations. The offset is also large, 0.4–0.5 dex, when compared with that provided by the models.

The very interesting point here is that Pilyugin method is giving the best results when it is applied for real objects for which the oxygen abundance has been computed using the T_e method (e.g. Bresolin et al. 2009; López-Sánchez & Esteban 2010; Moustakas et al. 2010). However, this method is clearly failing when predicting the metallicities of the theoretical models using the bright emission lines. We will further discuss this issue in Section 4.2.

4.1.4 Kewley and Dopita methods

Although the Pilyugin method considers a parameter which is related to the ionization degree of the gas, the scatter provided by this calibration is still relatively high. However, the scatter is much reduced when using a SEL method which is based on photoioniza-tion models, as those provided by the McGaugh (1991), Kewley & Dopita (2002) and Kobulnicky & Kewley (2004) methods. All these models explicitly consider an ionization parameter, *y*. Fig. 11 shows their results. As we see, in all these cases the agreement is excellent. We remind the reader that we are plotting both the high- and low-metallicity results for the models with 12+log(O/H) = 8.39.

The left-most panel of Fig. 11 shows the case of the McGaugh (1991) calibration using the Kobulnicky et al. (1999) parametriza-tion. This calibration systematically underestimates the abundances given by the models by ∼0.15 dex, but their dispersion is only
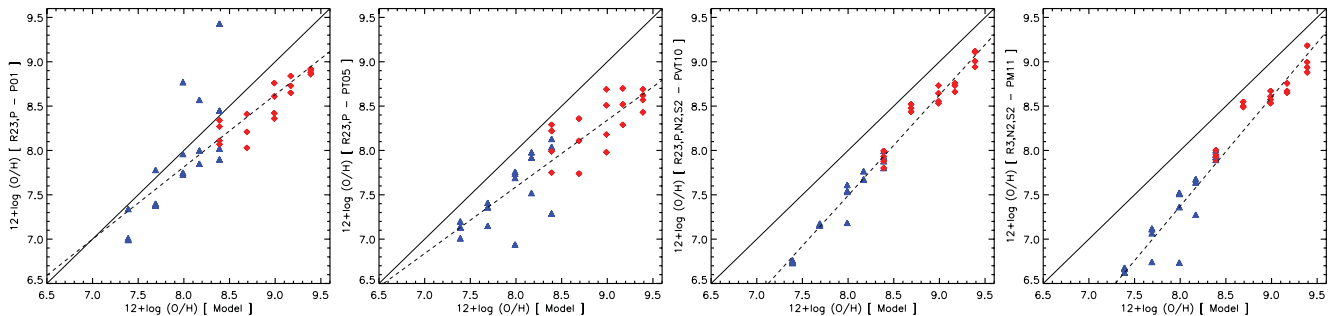
Figure 10. Comparison between the abundances used for the models (*x*-axis) and those computed via the Pilyugin method using the R_{23} and P parameters. From left to right, panels show the results for the empirical calibrations provided by Pilyugin (2001a,b), Pilyugin & Thuan (2005), Pilyugin et al. (2010) and Pilyugin & Mattsson (2011). The continuous line represents $y = x$. Red diamonds and blue triangles represent high- and low-metallicity models, respectively. The dashed line indicates the fit to the data. Note that, in the left-hand panel, the three data points with SEL abundances very much larger than those of the models are in the intermediate-metallicity regime and also have a relatively large log *q*. Hence, following the Pilyugin (2001a,b) method the high-metallicity calibration should be considered and averaged to the value derived using the low-metallicity calibration to get a more appropriate result for the oxygen abundance.
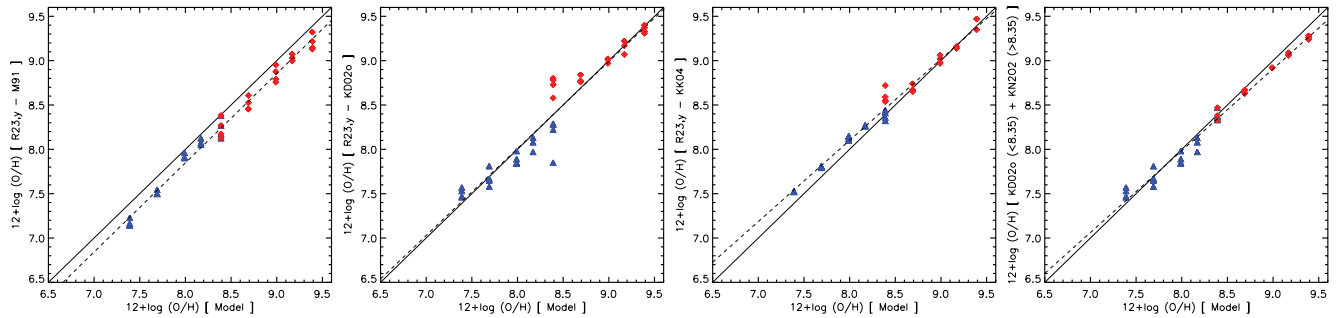
Figure 11. Comparison between the total abundances used for the models (*x*-axis) and those computed using the McGaugh (1991) method (left-most panel) and the Kewley & Dopita (2002) and Kobulnicky & Kewley (2004) techniques, all of them based on photoionization models. The continuous line represents $y = x$. Red diamonds and blue triangles represent high- and low-metallicity models, respectively. The dashed line indicates the fit to the data. The right-most panel shows the comparison with the oxygen abundance considering the N_2O_2 method for the high-metallicity branch, $12+\log(O/H) \geq 8.35$, and R_{23} and q_{KD02o} for the low-metallicity branch, following Kewley & Dopita (2002).

Table 5. Results of the comparison between the oxygen abundance given by several SEL methods and the oxygen abundance assumed by the theoretical models. We indicate the parameters, *a* and *b*, of the linear fit $x_{SEL} = a + bx_{model}$, the correlation coefficient, *r*, of this linear fit, the dispersion of the data, σ, and the average value of the difference between the abundance given by the SEL method and that assumed by the model. In the first row, we also include the comparison with the oxygen abundance derived following the T_e method. The description of the SEL methods is the same as that used in Table 4.

Method	*a*	*b*	*r*	σ	Offset
T_e	-0.02 ± 0.14	1.001 ± 0.017	0.9959	0.05	-0.01
M91	-0.20 ± 0.17	1.005 ± 0.020	0.9940	0.07	-0.15
KD02	0.16 ± 0.21	0.981 ± 0.025	0.9897	0.10	0.00
KN2O2	0.94 ± 0.18	0.887 ± 0.020	0.9960	0.05	-0.07
KK04	0.77 ± 0.10	0.916 ± 0.012	0.9975	0.07	0.07
KD	0.61 ± 0.16	0.922 ± 0.019	0.9932	0.09	-0.05
P01	1.30 ± 0.64	0.814 ± 0.075	0.8890	0.31	-0.25
PT05	1.58 ± 0.51	0.752 ± 0.061	0.9113	0.28	-0.50
PVT10	-1.58 ± 0.24	1.134 ± 0.029	0.9901	0.14	-0.44
PM11	-2.46 ± 0.44	1.229 ± 0.052	0.9736	0.25	-0.52
D02	2.11 ± 0.45	0.736 ± 0.055	0.9390	0.20	-0.04
PP04a	3.43 ± 0.35	0.575 ± 0.043	0.9392	0.25	-0.04
PP04b	3.39 ± 0.43	0.578 ± 0.052	0.9141	0.26	-0.05
PP04c	1.81 ± 1.04	0.767 ± 0.116	0.8548	0.19	-0.25
S_{23}	-1.47 ± 0.66	1.186 ± 0.081	0.9481	0.24	0.04
$S_{23}O_{23}$	-1.76 ± 0.67	1.208 ± 0.076	0.9641	0.17	0.07

0.07 dex. In the case of using the Kewley & Dopita (2002) or the Kobulnicky & Kewley (2004) method considering the R_{23} and *y* parameters, the results are much better. Their methods allow the ionization parameter and the oxygen abundance to be determined iteratively. Both the techniques by Kewley & Dopita and by Kobulnicky & Kewley eliminate the scatter in the SEL technique to a very large extent. For the Kewley & Dopita (2002) technique it is ∼0.1 dex, while for the Kobulnicky & Kewley (2004) technique it is ∼0.07 dex excepting the ambiguous region around $12+\log(O/H) = 8.4$.

The right-most panel of Fig. 11 shows a fit using the N_2O_2 calibration provided by Kewley & Dopita (2002) for the high-metallicity branch, $12+\log(O/H) \geq 8.35$, and relied on R_{23} and the technique they use for obtaining the ionization parameter for the lower metallicities. This assumption provides very good results, as this method has a very low offset, 0.05 dex, and dispersion, 0.09 dex.

The slight offset in the abundances derived following the Kewley & Dopita (2002) and Kobulnicky & Kewley (2004) methods is probably due to the fact that they used a different grid of models. The models we use in this paper are more closely related to the earlier Kewley & Dopita (2002) grid, except in respect of the much more sophisticated treatment of dust physics employed here.

However, the recent analysis of the ionized gas within a sample of ∼40 strong star-forming galaxies performed by López-Sánchez & Esteban (2010) shows that the oxygen abundances provided by photoionization models (McGaugh 1991; Kewley & Dopita 2002; Kobulnicky & Kewley 2004) are, systematically, 0.2–0.3 dex higher than the oxygen abundances provided by the T_e method. This observational result has been also found by Yin et al. (2007), Bresolin et al. (2009), Moustakas et al. (2010) and López-Sánchez et al. (2011); in some objects the differences reach up to 0.6 dex. Interestingly, however, the photoionization models developed by Dors et al. (2011) provided O/H values close to those obtained using the T_e method. Detailed tailor-made photoionization models of individual galaxies (e.g. Pérez-Montero et al. 2010) also provided results similar to those derived from the observed electron temperatures of the ionized gas.

4.2 Comparison of the SEL techniques with real data

Hence, we have further investigated the validity of the SEL techniques using real data. For this, we aim to use the deepest, highest quality observational data of Galactic and extragalactic H ɪɪ regions nowadays available. Particularly, we also want to compare the results provided by the T_e and the most common SEL techniques (the Pilyugin and the Kewley & Dopita methods) with the oxygen abundances derived using oxygen RLs. As is well known (e.g. Esteban et al. 2002, 2004, 2009; Peimbert 2003; García-Rojas et al. 2004, 2005; García-Rojas & Esteban 2007; Peimbert et al. 2007), in all cases the oxygen abundances determined using the RL method are 0.2–0.3 dex higher than the oxygen abundances derived using the T_e method, which is based on collisionally excited lines (CELs). The effect does not depend on metallicity, electron density, electron and Balmer temperatures or ionization degree (García-Rojas & Esteban 2007; Mesa-Delgado et al. 2009a), and it may be attributed to the presence of temperature fluctuations in H ɪɪ regions.

Moreover, recent analyses (Peimbert, Peimbert & Ruiz 2005; Przybilla, Nieva & Butler 2008; Simón-Díaz & Stasińska 2011) have found that the oxygen nebular abundance based on the RL method agrees better with the abundances of the stars associated with the nebulae than the one derived from the T_e method,

Table 6. Results of the oxygen abundances given by the T_e, RL, P and KD methods for Galactic (G) and extragalactic (E) H II regions for which oxygen RLs have been detected.

| Object	R_2	R_3	$\log N_2$	T_e	RL	P	KD	Type	Ref
M 42	2.981	0.375	−1.247	8.51 ± 0.03	8.71 ± 0.03	8.57	8.77	G	E04
NGC 3576	4.169	2.447	−0.767	8.56 ± 0.03	8.74 ± 0.06	8.51	8.80	G	GR04
S 311	1.318	5.591	−1.720	8.39 ± 0.05	8.54 ± 0.10	8.28	8.65	G	GR05
M 16	0.668	3.547	−2.055	8.56 ± 0.07	8.81 ± 0.07	8.45	8.79	G	GR06
M 20	0.350	0.009	−0.549	8.53 ± 0.06	8.71 ± 0.07	8.45	8.93	G	GR06
NGC 3603	0.828	0.389	−1.932	8.46 ± 0.05	8.72 ± 0.05	8.45	8.68	G	GR06
M 8	3.038	5.002	−1.184	8.51 ± 0.05	8.71 ± 0.04	8.50	8.95	G	GR07
M 17	3.038	5.002	−1.184	8.52 ± 0.04	8.76 ± 0.04	8.58	8.78	G	GR07
30 Dor	1.823	1.109	−0.692	8.33 ± 0.02	8.54 ± 0.05	8.39	8.63	E	Pe03
N11 B	1.925	5.728	−1.502	8.41 ± 0.00	8.74 ± 0.00	8.43	8.80	E	T03
N 66	2.052	6.349	−1.360	8.11 ± 0.00	8.47 ± 0.00	8.10	8.40	E	T03
NGC 6822V	3.000	3.764	−1.296	8.08 ± 0.03	8.37 ± 0.09	8.09	8.39	E	PPR05
NGC 5253A	2.429	3.860	−1.020	8.18 ± 0.04	8.42 ± 0.13	8.12	8.48	E	LS07
NGC 5253B	1.538	0.091	−0.430	8.19 ± 0.04	8.37 ± 0.10	8.12	8.47	E	LS07
NGC 5253C	0.554	1.229	−2.160	8.28 ± 0.04	8.53 ± 0.09	8.30	8.59	E	LS07
NGC 595	0.596	0.287	−0.792	8.45 ± 0.03	8.69 ± 0.05	8.51	8.72	E	E09
NGC 604	0.255	0.032	−0.627	8.38 ± 0.02	8.60 ± 0.03	8.61	8.73	E	E09
H 1013	1.038	1.178	−0.938	8.45 ± 0.06	8.73 ± 0.09	8.62	8.90	E	E09
NGC 5461	0.121	0.030	−0.865	8.41 ± 0.03	8.49 ± 0.06	8.56	8.73	E	E09
VS 44	1.603	0.690	−1.618	8.36 ± 0.02	8.61 ± 0.04	8.59	8.72	E	E09
NGC 2363	4.134	1.111	−1.096	7.76 ± 0.02	8.04 ± 0.05	7.71	8.10	E	E09
K 932	1.085	2.203	−1.842	8.41 ± 0.02	8.62 ± 0.03	8.52	8.77	E	E09

References. E04: Esteban et al. (2004); E09: Esteban et al. (2009); GR04: García-Rojas et al. (2004); GR05: García-Rojas et al. (2005); GR06: García-Rojas et al. (2006); GR07: García-Rojas & Esteban (2007); LS07: López-Sánchez et al. (2007); Pe03: Peimbert (2003); PPR05: Peimbert, Peimbert & Ruiz (2005); T03: Tsamis et al. (2003).

suggesting that RL abundances are more reliable than the abundances derived from CEL.

Table 6 lists all the 22 Galactic and extragalactic H II regions found in the literature for which oxygen abundances are available using both the RL and the T_e methods. Indeed, the average offset between T_e and RL abundances is 0.22 dex. Table 6 also compiles the derived R_{23}, P, y and N_2 indices derived from the reddening-corrected data. We must emphasize that, in almost all the cases, the error in the [O II] $\lambda\lambda$3726, 3729 lines is less than 5 per cent. Using these observational parameters, we then applied the Pilyugin et al. method and the Kewley & Dopita method to determine the oxygen abundances using these SEL techniques. Table 6 compiles the average value derived for the Pilyugin (2001a,b), Pilyugin & Thuan (2005) and Pilyugin et al. (2010) techniques (P) and the average value obtained for the Kewley & Dopita (2002) (using the R_{23}, y and N_2O_2 parameters) and the Kobulnicky & Kewley (2004) methods (KD).

As we see in Table 6, we find again that the results obtained using the P technique agree quite well with the oxygen abundance determined using the T_e method (offset of 0.03 dex), but the results provided by the KD method are systematically ∼0.30 dex larger. That is exactly the opposite behaviour we discussed in the previous section. This result is graphically shown in Fig. 12, which compares the T_e abundance (x-axis) with the oxygen abundances derived from the RL method (black squares), the P method (blue diamonds) and the KD technique (red triangles).

Interestingly, the results provided using the KD technique have a better agreement with the values determined from the RL method. These are systematically ∼0.08 dex lower than the oxygen abundances given by the KD method, but both agree within the errors (the dispersion of the RL data is ∼0.06 dex, while the dispersion of the KD data is ∼0.07 dex). This observational result, which was
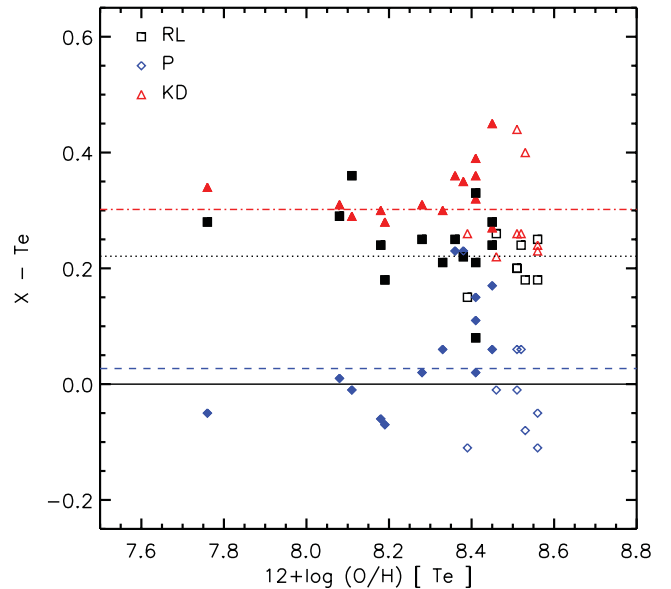
Figure 12. Comparison between the oxygen abundances derived following the T_e, RL, P and KD methods for deep, high-resolution observations of Galactic (open symbols) and extragalactic (filled symbols) H II regions for which oxygen RLs have been detected. The x-axis plots the T_e abundance, where the y-axis represents the difference between RL (black squares), P (blue diamonds) or KD (red triangles) abundances and the T_e abundance. The black dotted line plots the average difference between the T_e and the RL methods. The blue dashed line represents the average difference between the T_e and the P methods. The red dot–dashed line represents the average difference between the T_e and the KD methods.

previously noted by Peimbert et al. (2007) and López-Sánchez & Esteban (2010), is actually suggesting that the real metallicities of the H II regions may not be those given by the standard T_e method based on line ratios of CELs, but the values derived using the RL method. If this is correct, then the KD method is the only SEL technique that is reproducing those metallicities.

As we have seen in this paper, the oxygen abundances of our model spectra are well reproduced using the T_e method and SEL techniques based on photoionization models (McGaugh 1991; Kewley & Dopita 2002; Kobulnicky & Kewley 2004) but 0.3–0.5 dex higher than those estimated using the Pilyugin method. However, the situation is inverted in other works based on the comparison of observations with the results of the SEL methods (e.g. Peimbert et al. 2007; Yin et al. 2007; Bresolin et al. 2009; López-Sánchez & Esteban 2010; Moustakas et al. 2010; López-Sánchez et al. 2011; Rosales-Ortega et al. 2011), i.e. the oxygen abundance in real nebulae is better reproduced by those SEL methods which rely on an empirical calibration derived using H II regions where a direct estimation of the electron temperature exists.

A possible explanation of this puzzling situation is that current photoionization models are not properly reproducing the behaviour of CELs in real nebulae. As we said before, several authors have invoked the presence of temperature fluctuations in the nebulae (Peimbert 1967) in order to address the differences between the abundances determined from CELs and RLs. Due to the strong dependence of the intensity of CELs on T_e, such temperature fluctuations cause the metallicities derived from CELs to be underestimated. Although our models consider global temperature gradients due to the hardening of the ionizing radiation field along the nebula, they did not reproduce the values of the temperature fluctuation parameter (t^2) that are necessary to make the O/H ratios determined from RLs and CELs converge (e.g. García-Rojas & Esteban 2007). These hypothetical fluctuations must be of small spatial scale and may be produced by, for example, density inhomogeneities or localized deposition of mechanical energy that heats the gas.

Summarizing, assuming the validity of the scenario outlined above, the oxygen abundances determined from RLs and using SEL techniques based on photoionization models (KD method) would be closer to the real ones, while values determined from CELs and empirical calibrations (P method) would provide abundances about 0.2–0.3 dex lower. This should have a profound impact in current galaxy metallicity estimations that have been obtained using CELs or any empirical calibration – such as those provided by Pilyugin et al. or Pettini & Pagel (2004) – that should be revised upwards.

Finally, we want to note that the small offset of ∼0.08 dex between the RL and the KD methods may be a consequence of the depletion of the oxygen atoms in dust grains. Our models are taking into account this effect, but observations suggest that oxygen depletion in dust grains may be decreasing the actual gas-phase metallicity (i.e. that derived from the RL method) of H II regions by 0.08–0.12 dex (Mesa-Delgado et al. 2009b; Peimbert & Peimbert 2010; Simón-Díaz & Stasińska 2011).

5 CONCLUSIONS

In this paper, we have subjected the commonly used techniques for deriving chemical abundances to a critical 'double-blind' analysis. We find that the originally used T_e method is capable of delivering reliable abundances for O, N, S and Cl. However, the abundances inferred for the noble gases Ne and Ar are considerably less secure, although probably for different physical reasons.

The electron temperature itself is a reasonably good indicator of the oxygen abundance, as one is the dominant controller of the other. Error arises because there is also a weaker dependence of electron temperature on the ionization parameter. For the [O III] lines, this renders an abundance obtained from the electron temperature alone unreliable below $12+\log(O/H) \lesssim 8.0$.

The temperature derived from the temperature-sensitive CEL ratios is always somewhat different from emission-weighted temperature defined for the principal emission lines: $\lambda4959 + \lambda5007$ in the case of [O III]. This is due to the variability of electron temperature through the zone containing the ion of interest due to hardening of the radiation field and spherical divergence of the radiation field (which changes the photoelectric heating rate), and change in ionization state (which influences the cooling rate of the plasma). In this sense, the models naturally produce electron temperature gradients inside H II regions, such as those discussed in Stasińska (1978, 2005) and Garnett (1992).

Although our models can reproduce these 'global' temperature fluctuations, they cannot simulate the small-scale temperature fluctuations, such as those first discussed by Peimbert (1967) and Peimbert & Costero (1969), produced by turbulent or photoevaporative flows, shocks or radiation shielding by dense inclusions or globules of unionized material. Thus we can be reasonably sure that the true temperature fluctuations in real H II regions should be greater than the models predict. The effect of this would be to raise the temperature as measured by [O III] $(\lambda4959+\lambda5007)/\lambda4363$, which would then feed into a systematic underestimate in the oxygen abundance as delivered by the T_e method. Hence, accepting the existence of small-scale temperature fluctuations within the ionized gas and assuming that the RLs give the true metallicities, those oxygen abundances determined from CELs and empirical calibrations (P method) would provide abundances which are 0.2–0.3 dex lower than the real ones. That is because of the strong dependence of the intensity of CELs on T_e: the existence of such small-scale temperature fluctuations will cause an underestimation of the oxygen abundances using CEL lines or strong-line methods which are based on the bright nebular lines. However, oxygen abundances derived using SEL techniques based on photoionization models (such as the KD method, for which the T_e is fixed a priori) would be closer to the real values.

We have demonstrated that those SEL techniques that do not explicitly solve for the ionization parameter are quite unreliable, resulting in large scatter, systemic error and abundance-dependent errors. To obtain the ionization parameter, we need a measurement of the [O III] $\lambda5007$/[O II] $\lambda3726, 3729$ ratio. For abundances $12+\log(O/H) \lesssim 8.0$, the oxygen abundance could then be estimated from the [O III] $\lambda5007$/Hβ line ratio. This is verified in Fig. 13, which provides a new diagnostic plot for this low-abundance regime.

At high abundance, the most sensitive diagnostic plot is that of [O III] $\lambda5007$/[O II] $\lambda3726, 3729$ versus [N II] $\lambda6584$/[O II] $\lambda3726, 3729$, shown in Fig. 1(c). The main error here is the degree to which the N/O abundance has been accurately calibrated against the O abundance. We believe that the relationship given in equation (1) is probably good, since the model grids reproduce the Veilleux & Osterbrock (1987) diagnostic plots shown in Figs 1(a) and (b).

Figs 1(c) and 13 thus provide a SEL technique that is applicable to the determination of both metallicity and ionization parameter over the full abundance range, with the caveat that the sensitivity of this technique is rather poor in the range $8.0 \lesssim 12 + \log(O/H) \lesssim 8.4$. In this range, common to all SEL techniques, rather accurately measured line ratios are required.
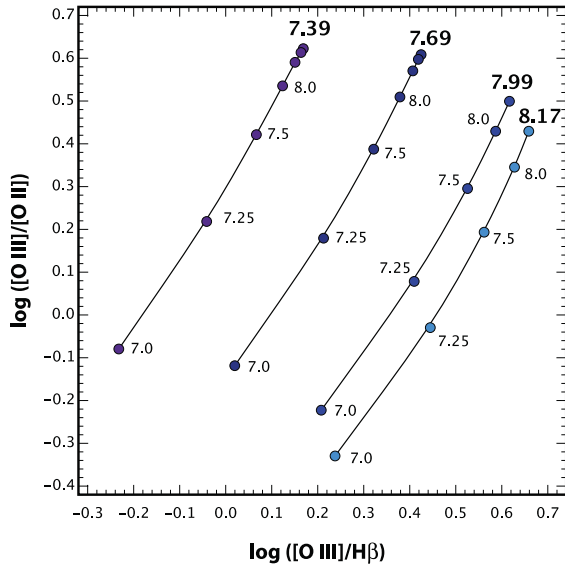
Figure 13. The model grid of [O III] λ5007/Hβ versus [O III] λ5007/[O II] $\lambda\lambda$3726, 3729 at the low-abundance end. This confirms that both 12 + log(O/H) and log q can be derived from this diagnostic diagram for 12 + log(O/H) $\lesssim$ 8.0.

REFERENCES

Abazajian K. et al., 2003, AJ, 126, 2081
Aller L. H., ed. 1984, Physics of Thermal Gaseous Nebulae. Reidel, Dordrecht
Alloin D., Collin-Souffrin S., Joly M., Vigroux L., 1979, A&A, 78, 200
Baldwin J., Phillips M. M., Terlevich R. J., 1981, PASP, 93, 5
Bresolin F., Schaerer D., González Delgado R. M., Stasińska G., 2005, A&A, 441, 981
Bresolin F., Gieren W., Kudritzki R.-P., Pietrzyński G., Urbaneja M. A., Carraro G., 2009, ApJ, 700, 309
Brinchmann J. et al., 2004, MNRAS, 351, 1151
Christensen T., Petersen L., Gammelgaard P., 1997, A&A, 322, 41
Davé R., Oppenheimer B. D., 2007, MNRAS, 374, 427
Denicoló G., Terlevich R., Terlevich E., 2002, MNRAS, 330, 69
Díaz A. I., Pérez-Montero E., 2000, MNRAS, 312, 130
Díaz A. I., Terlevich E., Pagel B. E. J., Vílchez J. M., Edmunds M. G., 1987, MNRAS, 226, 19
Dopita M. A., Kewley L. J., Heisler C. A., Sutherland R. S., 2000, ApJ, 542, 224
Dopita M. A. et al., 1997, ApJ, 474, 188
Dopita M. A. et al., 2006a, ApJS, 167, 177
Dopita M. A. et al., 2006b, ApJ, 647, 244
Dors O. L., Jr, Copetti M. V. F., 2006, A&A, 452, 473
Dors O. L., Jr, Krabbe A., Hägele G. F., Pérez-Montero E., 2011, MNRAS, 415, 3616
Esteban C., 2002, Rev. Mex Astron. Astrofis., 12, 56
Esteban C., Peimbert M., 1995, A&A, 300, 78
Esteban C., Peimbert M., Torres-Peimbert S., Escalante V., 1998, MNRAS, 295, 401

Esteban C., Peimbert M., Torres-Peimbert S., Rodríguez M., 2002, ApJ, 581, 241
Esteban C., Peimbert M., García-Rojas J., Ruiz M. T., Peimbert A., Rodríguez M., 2004, MNRAS, 355, 229
Esteban C., Bresolin F., Peimbert M., García-Rojas J., Peimbert A., Mesa-Delgado A., 2009, ApJ, 700, 654
Ferland G., Fabian A. C., Johnston R., 1994, MNRAS, 266, 399
Ferland G., 1995, in Williams R., Livio M., eds, The Analysis of Emission Lines: A meeting in Honor of the 70th Birthdays of D. E. Osterbrock & M. J. Seaton, p. 83
García-Rojas J., Esteban C., 2007, ApJ, 670, 457
García-Rojas J., Esteban C., Peimbert M., Rodríguez M., Ruiz M. T., Peimbert A., 2004, ApJS, 153, 501
García-Rojas J., Esteban C., Peimbert A., Peimbert M., Rodríguez M., Ruiz, 2005, MNRAS, 362, 301
García-Rojas J., Esteban C., Peimbert M., Costado M. T., Rodríguez M., Peimbert A., Ruiz M. T., 2006, MNRAS, 368, 253
Garnett D. R., 1992, AJ, 103, 1330
Grevesse N., Asplund M., Sauval A. J., Scott P., 2010, Ap&SS, 328, 179
Hägele G. F., Díaz Á. I., Terlevich E., Terlevich R., Pérez-Montero E., Cardaci M. V., 2008, MNRAS, 383, 209
Hägele G. F., García-Benito R., Pérez-Montero E., Díaz Á. I., Cardaci M. V., Firpo V., Terlevich E., Terlevich R., 2011, MNRAS, 414, 272
Izotov Y. I., Thuan T. X., Lipovetski, 1994, ApJ, 435, 647
Izotov Y. I., Stasińska G., Meynet G., Guseva N. G., Thuan T. X., 2006, A&A, 448, 955
Jensen E. B., Strom K. M., Strom S. E., 1976, ApJ, 209, 748
Kewley L. J., Dopita M. A., 2002, ApJS, 142, 35
Kewley L. J., Ellison S. E., 2008, ApJ, 681, 1183
Kewley L. J., Groves B., Kauffmann G., Heckman T., 2006, MNRAS, 372, 961
Kingdon J., Ferland G. J., 1995, ApJ, 442, 714
Kobulnicky H. A., Kewley L. J., 2004, ApJ, 617, 240
Kobulnicky H. A., Kennicutt R. C., Jr, Pizagno J. L., 1999, ApJ, 514, 544
Lara-López M. A., Bongiovanni A., Cepa J., Pérez García A. M., Sánchez-Portal M., Castañeda H. O., Fernández Lorenzo M., Pović M., 2010a, A&A, 519, 31
Lara-López M. A. et al., 2010b, A&A, 521, 53
Leitherer C. et al., 1999, ApJS, 123, 3
Levesque E. M., Kewley L. J., Larson K. L., 2010, AJ, 139, 712
López-Sánchez Á. R., Esteban C., 2009, A&A, 508, 615
López-Sánchez Á. R., Esteban C., 2010, A&A, 517, 85
López-Sánchez Á. R., Esteban C., García-Rojas J., Peimbert M., Rodríguez M., 2007, ApJ, 656, 168
López-Sánchez Á. R., Mesa-Delgado A., López-Martìn L., Esteban C., 2011, MNRAS, 411, 2076
McGaugh S. S., 1991, ApJ, 380, 140
Mesa-Delgado A., Esteban C., 2010, MNRAS, 405, 2651
Mesa-Delgado A., López-Martín L., Esteban C., García-Rojas & Luridiana V., 2009a, MNRAS, 394, 693
Mesa-Delgado A., Esteban C., García-Rojas, Luridiana V., Bautista M., Rodríguez M., López-Martín L., Peimbert M., 2009b, MNRAS, 395, 855
Mesa-Delgado A., Núñez-Díaz M., Esteban C., López-Martín L., García-Rojas J., 2011, MNRAS, 417, 420
Mollá M., Díaz A. I., 2005, MNRAS, 358, 521
Monreal-Ibero A., Vílchez J. M., Walsh J. R., Muñoz-Tuñón C., 2010, A&A, 517, 27
Moustakas J., Kennicutt R. C., Jr, Tremonti C. A., Dale D. A., Smith J.-D. T., Calzetti D., 2010, ApJS, 190, 233
Osterbrock D. E., Ferland G. J., 2006, Astrophysics of gaseous nebulae and active galactic nuclei, 2nd edn. University Science Books, Sausalito, CA
Pagel B. E. J., Edmunds M. G., Blackwell D. E., Chun M. S., Smith G., 1979, MNRAS, 189, 95
Peimbert M., 1967, ApJ, 150, 825
Peimbert A., 2003, ApJ, 584, 735

Peimbert M., Costero R., 1969, Bol. Obs. Tonantzintla Tacubaya, 5, 3
Peimbert M., Peimbert A., 2006, in Barlow M. J., Méndez R. H., eds, Proc. IAU Symp. 234, Planetary Nebulae in Our Galaxy and Beyond. Cambridge Univ. Press, Cambridge, p. 227
Peimbert A., Peimbert M., 2010, ApJ, 724, 791
Peimbert M., Torres-Peimbert S., 1977, MNRAS, 179, 217
Peimbert A., Peimbert M., Ruiz M. T., 2005, ApJ, 634, 1056
Peimbert M., Peimbert A. Esteban C., García-Rojas J., Bresolin F., Carigi L., Ruiz M. T., López-Sánchez Á. R., 2007, Rev. Mex. Astron. Astrofis., 29, 72
Pérez-Montero E., Contini T., 2009, MNRAS, 398, 949
Pérez-Montero E., Díaz Á. I., 2005, MNRAS, 361, 1063
Pérez-Montero E., Hägele G. F., Contini T., Díaz Á. I., 2007, MNRAS, 381, 125
Pérez-Montero E., García-Benito R., Hägele G. F., Díaz Á. I., 2010, MNRAS, 404, 2037
Pettini M., Pagel B. E. J., 2004, MNRAS, 348, 59
Pilyugin L. S., 2000, A&A, 362, 325
Pilyugin L. S., 2001a, A&A, 369, 594
Pilyugin L. S., 2001b, A&A, 374, 412
Pilyugin L. S., Mattsson L., 2011, MNRAS, 412, 1145
Pilyugin L. S., Thuan T. X., 2005, ApJ, 631, 231
Pilyugin L. S., Víchez J. M., Thuan T. X., 2010, ApJ, 720, 1738
Przybilla N., Nieva M.-F., Butler K., 2008, ApJ, 688, 103
Pustilnik S., Kniazev A., Pramskij A., Izotov Y., Foltz C., Brosch N., Martin J.-M., Ugryumov A., 2004, A&A, 419, 469
Rodríguez M., García-Rojas G., 2010, ApJ, 708, 1551
Rosales-Ortega F. F., Díaz A. I., Kennicutt R. C., Sánchez S. F., 2011, MNRAS, 415, 2439

Shaw R. A., Dufour R. J., 1995, PASP, 107, 896
Simón-Díaz S., Stasińska G., 2011, A&A, 526, 48
Stasińska G., 1978, A&A, 66, 257
Stasińska G., 2002, Rev. Mex. Conf. Ser., 12, 62
Stasińska G., 2005, A&A, 434, 507
Sutherland R. S., Dopita M. A., 1993, ApJS, 88, 253
Tremonti C. A. et al., 2004, ApJ, 613, 898
Tsamis Y. G., Barlow M. J., Liu X.-W., Danziger I. J., Storey P. J., 2003, MNRAS, 338, 687
Vázquez G. A., Leitherer C., 2005, ApJ, 621, 695
Veilleux S., Osterbrock D. E., 1987, ApJS, 63, 295
Vílchez J. M., Esteban C., 1996, MNRAS, 280, 720
Yin S. Y., Liang Y. C., Hammer F., Brinchmann J., Zhang B., Deng L. C., Flores H., 2007, A&A, 462, 535
York D. G. Jr, et al., 2000, AJ, 120, 1579

APPENDIX A: ELECTRON TEMPERATURES, ELECTRON DENSITIES AND IONIC ABUNDANCES FOR THE MODEL H II REGIONS

Here we compile the derived parameters for the model H II regions. The first table, Table A1, gives the derived densities and temperatures in the various zones of the H II region. Table A2 gives the derived ionic abundances. Finally, Table A3 gives the line ratio values used to compute the oxygen abundance using the empirical calibrations as well as the ionization parameters derived for the models using the Kewley & Dopita (2002) and Kobulnicky & Kewley (2004) techniques.

Table A1. Electron density and temperature obtained from the analysis of emission-line ratios of model spectra using the IRAF task temden.

Model	[S II]	[O II]	[N I]	[Cl III]	Adopted	[O III]	[S III]	[Ar III]	Adopted	[O II]	[S II]	[N II]	Adopted
			n_e (cm^{-2})					T_e(high) (K)				T_e(low) (K)	
A	6	213	12	113	**86**	8465	8037	8389	**8297**	8419	6419	9274	**8037**
B	0	243	7	136	**96**	14947	12222	13307	**13492**	12141	7621	13658	**11140**
C	30	0	0	68	**49**	0	4425	4519	**4472**	0	3843	4680	**4261**[a]
D	0	236	7	135	**126**	12663	11009	11706	**11792**	11122	7337	12820	**10426**
E	0	228	8	130	**122**	11459	10134	10732	**10775**	10311	7086	11802	**9733**
F	0	226	9	130	**121**	10498	9625	10159	**10094**	9834	7023	11254	**9370**
G	25	182	23	76	**76**	4855	4993	4908	**4918**	5423	4535	5660	**5206**
H	33	0	0	68	**50**	4285	4210	4236	**4243**	0	3737	4474	**4105**[a]
I	19	196	21	87	**80**	5830	5873	5973	**5892**	6424	5313	6986	**6241**
J	35	0	0	71	**53**	0	3910	3768	**3839**	0	3633	4269	**3951**[a]
K	0	234	7	135	**125**	12413	10843	11519	**11591**	10968	7304	12633	**10301**
L	0	229	8	130	**122**	11394	10139	10737	**10756**	10297	7122	11796	**9738**
M	0	240	7	138	**128**	13637	11749	12613	**12666**	11614	7514	13408	**10845**
N	6	214	12	113	**86**	8129	7811	8144	**8028**	8409	6435	9280	**8041**
O	21	182	21	77	**75**	5769	5542	5665	**5658**	5681	4660	5996	**5445**
P	0	241	7	138	**128**	14096	12034	12953	**13027**	11833	7556	13658	**11015**
Q	0	239	7	135	**127**	13718	11640	12568	**12642**	11462	7454	13202	**10706**
R	16	194	19	86	**78**	6225	6158	6283	**6222**	6549	5322	6996	**6289**
S	0	232	8	135	**125**	11890	10586	11248	**11241**	10661	7284	12268	**10071**
T	0	234	8	136	**126**	12181	10781	11506	**11489**	10804	7314	12451	**10189**
U	0	228	9	131	**122**	10525	9641	10182	**10116**	9913	7044	11364	**9440**
V	0	241	7	139	**129**	14562	12172	13223	**13319**	11840	7525	13640	**11001**
W	0	225	9	129	**121**	10537	9589	10116	**10080**	9748	6962	11119	**9276**
X	40	0	0	78	**59**	0	3930	0	**3930**	0	3695	4338	**4016**[a]
Y	0	243	7	136	**128**	15740	12547	13728	**14005**	12101	7554	13892	**11182**
Z	13	194	17	90	**78**	6941	6580	6790	**6770**	6768	5356	7252	**6458**
AA	22	181	23	75	**75**	5364	5295	5338	**5332**	5498	4588	5788	**5291**
AB	0	234	8	135	**125**	12452	10927	11628	**11669**	11001	7359	12678	**10346**
AC	15	194	17	89	**78**	6741	6483	6654	**6626**	6712	5378	7189	**6426**
AD	0	243	6	138	**129**	15240	12497	13644	**13793**	12078	7563	13888	**11176**
AE	0	238	7	139	**128**	13248	11484	12330	**12354**	11363	7459	13115	**10645**
AF	0	222	10	125	**119**	10289	9308	9814	**9803**	9470	6799	10740	**9003**
AG	5	212	12	113	**85**	8765	8182	8545	**8497**	8477	6389	9318	**8061**

[a]The ionic task does not allow electron temperatures lower than 5000 K for the low-ionization ions, so we adopted T_e(low) = 5000 K for these cases.

Table A2. Ionic abundances derived for the results of the photoionization models using the IRAF task ionic considering the electron temperature derived from all the high-ionization species, T_e(high), and the low-ionization species, T_e(low), separately. All numbers are expressed in the form of 12+log (X/H).

Model		O^+/H^+	O^{++}/H^+	N^+/H^+	S^+/H^+	S^{++}/H^+	Ne^{++}/H^+	Ar^+/H^+	Ar^{++}/H^+	Cl^{++}/H^+	Cl^{3+}/H^+
A		8.717	8.126	7.333	6.327	7.074	7.683	6.458	4.364	4.272	3.578
	disp.	0.031	0.016	0.085	0.095	0.018	0.071	0.007	0.001	0.001	0.090
B		7.283	7.609	5.635	4.928	5.873	6.941	5.326	4.915	2.810	3.251
	disp.	0.036	0.049	0.084	0.122	0.036	0.071	0.006	0.000	0.001	0.090
C		8.873	7.101	8.257	7.224	7.365	7.347	6.586	0.000	4.575	2.487
	disp.	0.115	4.100	0.070	0.189	0.011	0.071	0.013	0.000	0.001	0.090
D		7.489	6.809	5.840	5.208	5.727	6.468	5.132	2.969	2.882	2.502
	disp.	0.029	0.039	0.091	0.119	0.028	0.071	0.004	0.001	0.000	0.090
E		8.173	6.915	6.606	6.003	6.282	6.884	5.703	2.871	3.517	2.695
	disp.	0.029	0.037	0.092	0.113	0.028	0.071	0.003	0.001	0.000	0.090
F		8.252	8.127	6.717	5.796	6.752	7.544	6.157	4.787	3.868	3.666
	disp.	0.026	0.026	0.091	0.106	0.625	0.071	0.003	0.001	0.000	0.090
G		9.089	8.315	8.038	6.764	7.525	7.803	6.747	4.544	4.725	3.535
	disp.	0.038	0.018	0.079	0.088	0.015	0.071	0.003	0.000	0.000	0.090
H		8.710	7.821	8.152	7.003	7.564	7.658	6.802	3.624	4.771	3.019
	disp.	0.144	0.017	0.122	0.219	0.008	0.071	0.002	0.000	0.001	0.090
I		8.963	8.309	7.709	6.447	7.240	7.754	6.559	4.909	4.416	3.763
	disp.	0.061	0.076	0.137	0.058	0.048	0.071	0.041	0.000	0.000	0.090
J		8.372	8.105	7.892	6.667	7.676	7.710	6.781	4.095	4.855	3.231
	disp.	0.170	4.680	0.178	0.238	0.022	0.071	0.028	0.002	0.001	0.090
K		7.778	7.081	6.155	5.502	6.028	6.754	5.433	3.223	3.194	2.765
	disp.	0.026	0.039	0.087	0.120	0.028	0.071	0.004	0.001	0.000	0.090
L		8.313	7.388	6.758	6.015	6.505	7.129	5.905	3.456	3.711	3.024
	disp.	0.028	0.035	0.091	0.112	0.027	0.071	0.002	0.001	0.000	0.090
M		7.536	7.470	5.884	5.167	6.022	6.876	5.431	4.191	3.036	3.096
	disp.	0.029	0.038	0.089	0.120	0.029	0.071	0.003	0.001	0.000	0.090
N		8.481	8.378	7.079	6.029	7.065	7.804	6.458	5.041	4.216	3.858
	disp.	0.031	0.010	0.085	0.094	0.016	0.071	0.010	0.001	0.001	0.090
O		9.185	7.426	8.201	7.180	7.307	7.405	6.597	3.204	4.517	2.846
	disp.	0.025	0.000	0.047	0.119	0.034	0.071	0.018	0.000	0.000	0.090
P		7.218	7.183	5.548	4.862	5.712	6.581	5.124	3.946	2.705	2.818
	disp.	0.030	0.039	0.089	0.122	0.030	0.071	0.003	0.001	0.000	0.090
Q		7.644	7.880	6.022	5.232	6.224	7.223	5.667	5.094	3.210	3.505
	disp.	0.029	0.042	0.090	0.120	0.032	0.071	0.003	0.001	0.000	0.090
R		8.984	8.338	7.788	6.615	7.368	7.862	6.711	4.579	4.579	3.652
	disp.	0.034	0.001	0.082	0.089	0.008	0.071	0.009	0.000	0.000	0.090
S		8.110	7.855	6.516	5.674	6.535	7.300	5.927	4.379	3.643	3.414
	disp.	0.027	0.033	0.090	0.112	0.026	0.071	0.001	0.001	0.000	0.090
T		7.896	8.008	6.297	5.444	6.472	7.373	5.896	5.017	3.510	3.603
	disp.	0.027	0.033	0.090	0.114	0.027	0.071	0.001	0.001	0.000	0.090
U		8.067	8.227	6.531	5.607	6.692	7.596	6.117	5.290	3.755	3.812
	disp.	0.026	0.026	0.091	0.107	0.023	0.071	0.003	0.002	0.000	0.090
V		7.349	7.579	5.698	4.983	5.921	6.924	5.369	4.758	2.868	3.221
	disp.	0.030	0.043	0.089	0.123	0.033	0.071	0.004	0.001	0.000	0.090
W		8.481	7.804	6.972	6.106	6.759	7.406	6.150	3.992	3.946	3.351
	disp.	0.026	0.029	0.091	0.107	0.024	0.071	0.002	0.001	0.000	0.090
X		8.199	7.632	7.698	6.368	7.457	7.095	6.138	3.674	4.599	2.834
	disp.	0.152	4.407	0.159	0.227	0.000	0.071	0.607	0.003	0.000	0.090
Y		7.004	7.312	5.337	4.657	5.561	6.641	5.015	4.628	2.484	2.956
	disp.	0.031	0.053	0.088	0.126	0.039	0.071	0.009	0.001	0.000	0.090
Z		9.179	7.161	8.024	7.151	7.158	7.350	6.502	2.898	4.387	2.758
	disp.	0.036	0.025	0.087	0.098	0.020	0.071	0.002	0.001	0.001	0.090
AA		9.292	8.103	8.240	7.056	7.484	7.746	6.769	4.105	4.698	3.336
	disp.	0.037	0.008	0.083	0.090	0.006	0.071	0.001	0.000	0.000	0.090
AB		8.016	7.570	6.405	5.639	6.349	7.093	5.742	3.905	3.478	3.168
	disp.	0.028	0.036	0.090	0.116	0.027	0.071	0.002	0.001	0.000	0.090
AC		9.138	7.906	7.964	6.903	7.303	7.666	6.654	3.869	4.529	3.294
	disp.	0.035	0.017	0.084	0.093	0.016	0.071	0.003	0.001	0.001	0.090

Table A2 – *continued*

Model		O$^+$/H$^+$	O^{++}/H$^+$	N$^+$/H$^+$	S$^+$/H$^+$	S^{++}/H$^+$	Ne^{++}/H$^+$	Ar$^+$/H$^+$	Ar^{++}/H$^+$	Cl^{++}/H$^+$	Cl^{3+}/H$^+$
AD		7.042	7.285	5.374	4.690	5.604	6.625	5.055	4.492	2.535	2.931
	disp.	*0.031*	*0.047*	*0.089*	*0.125*	*0.035*	*0.071*	*0.005*	*0.001*	*0.000*	*0.090*
AE		7.766	7.814	6.141	5.348	6.304	7.189	5.722	4.717	3.322	3.422
	disp.	*0.028*	*0.037*	*0.090*	*0.118*	*0.029*	*0.071*	*0.002*	*0.001*	*0.000*	*0.090*
AF		8.585	7.112	7.118	6.439	6.669	7.157	6.084	3.024	3.914	2.857
	disp.	*0.027*	*0.033*	*0.091*	*0.107*	*0.026*	*0.071*	*0.001*	*0.001*	*0.000*	*0.090*
AG		8.851	7.570	7.503	6.639	7.005	7.456	6.400	3.515	4.239	3.153
	disp.	*0.033*	*0.024*	*0.085*	*0.098*	*0.021*	*0.071*	*0.004*	*0.001*	*0.001*	*0.090*

Table A3. Parameters used to compute the oxygen abundance using empirical calibrations.

Model	R_2	R_3	R_{23}	P	y	$\log N_2$	$\log O_3 N_2$	$\log O_2 N_2$	S_2	S_{23}	$\log q_{KD02}$[a]	$\log q_{KK04}$[b]
A	4.169	2.447	6.616	0.370	−0.231	−0.640	1.026	1.387	0.623	2.445	7.72	7.32
B	0.668	3.547	4.215	0.842	0.725	−1.928	2.481	1.880	0.060	0.367	8.40	7.87
C	0.350	0.009	0.359	0.025	−1.583	−0.422	−1.619	0.093	1.001	1.560	6.69	6.47
D	0.828	0.389	1.216	0.319	−0.329	−1.805	1.397	1.850	0.098	0.269	7.16	7.13
E	2.981	0.375	3.356	0.112	−0.901	−1.120	0.691	1.721	0.510	1.028	7.30	6.87
F^c	3.038	5.002	8.040	0.622	0.217	−1.057	1.754	1.667	0.284	1.960	7.81	7.65, 7.74
G	0.596	0.287	0.883	0.325	−0.318	−0.665	0.120	0.567	0.352	1.452	7.47	7.83
H	0.255	0.032	0.288	0.112	−0.898	−0.500	−0.993	0.034	0.620	1.337	6.78	7.52
I	1.038	1.178	2.215	0.532	0.055	−0.811	0.879	0.954	0.266	1.604	7.78	8.09
J	0.121	0.030	0.152	0.200	−0.603	−0.738	−0.783	−0.051	0.294	0.875	6.94	8.58
K	1.603	0.690	2.293	0.301	−0.366	−1.491	1.328	1.823	0.191	0.522	7.08	7.14
L	4.134	1.111	5.245	0.212	−0.571	−0.969	1.013	1.712	0.524	1.384	7.61	7.09
M	1.085	2.203	3.288	0.670	0.308	−1.715	2.056	1.877	0.098	0.481	8.00	7.56
N	2.429	3.860	6.289	0.614	0.201	−0.893	1.477	1.405	0.313	1.959	7.90	7.85
O	1.538	0.091	1.629	0.056	−1.227	−0.303	−0.739	0.617	1.397	2.610	6.87	6.99
P	0.554	1.229	1.782	0.689	0.346	−2.033	2.120	1.903	0.050	0.247	7.54	7.54
Q	1.318	5.591	6.909	0.809	0.627	−1.593	2.338	1.840	0.110	0.721	8.31	7.90
R	1.823	1.109	2.932	0.378	−0.216	−0.565	0.608	0.953	0.532	2.210	7.55	7.73
S	3.000	3.764	6.764	0.556	0.099	−1.169	1.742	1.773	0.260	1.262	7.94	7.53
T	1.925	5.728	7.653	0.748	0.473	−1.375	2.131	1.787	0.158	1.061	8.34	7.81
U^c	2.052	6.349	8.401	0.756	0.490	−1.233	2.034	1.672	0.188	1.356	8.37	7.85, 7.97
V	0.744	3.232	3.976	0.813	0.638	−1.883	2.390	1.882	0.066	0.400	8.32	7.80
W^c	4.906	2.354	7.260	0.324	−0.319	−0.814	1.183	1.632	0.565	1.919	7.62	7.28, 7.34
X	0.079	0.012	0.092	0.134	−0.812	−0.961	−1.002	−0.012	0.145	0.550	7.12	–
Y	0.357	1.968	2.325	0.846	0.741	−2.242	2.533	1.922	0.033	0.192	8.42	7.82
Z	3.360	0.107	3.467	0.031	−1.495	−0.288	−0.683	0.941	2.049	3.382	6.90	6.76
AA	1.085	0.275	1.361	0.202	−0.595	−0.434	−0.128	0.597	0.742	2.104	7.01	7.49
AB	2.707	2.180	4.887	0.446	−0.094	−1.257	1.593	1.816	0.257	0.959	7.91	7.36
AC	2.975	0.545	3.520	0.155	−0.737	−0.354	0.088	0.954	1.127	2.874	7.44	7.22
AD	0.389	1.796	2.185	0.822	0.664	−2.206	2.458	1.923	0.035	0.206	8.34	7.76
AE	1.710	4.535	6.245	0.726	0.424	−1.486	2.140	1.846	0.141	0.844	8.11	7.73
AF^c	5.403	0.431	5.834	0.074	−1.098	−0.709	0.342	1.569	1.125	2.169	8.18	6.82, 6.88
AG	5.738	0.737	6.475	0.114	−0.891	−0.465	0.330	1.351	1.296	2.945	7.15	6.98

[a]Value derived for the q parameter (in units of cm s^{-1}) obtained using the optimal calibration given by Kewley & Dopita (2002).
[b]Value derived for the q parameter (in units of cm s^{-1}) obtained using the iterative procedure described in Kobulnicky & Kewley (2004).
[c]For these models, for which we derived 12+log(O/H) ∼ 8.4 following the T_e method, we list the results of the empirical calibrations considering both the low- and the high-metallicity branches. The q_{KK04} parameters listed here for these models are for the low- and high-metallicity branches.

This paper has been typeset from a TEX/LATEX file prepared by the author.